A general analysis of Wtb anomalous couplings*

A general analysis of Wtb anomalous couplings *

Qing-Hong Cao(曹庆宏)[1,2,3;1)] Bin Yan(岩斌)[1;2)] Jiang-Hao Yu(于江浩)[4;3)] Chen Zhang(张宸)[1;4)]

[1] Department of Physics and State Key Laboratory of Nuclear Physics and Technology, Peking University, Beijing 100871, China
[2] Collaborative Innovation Center of Quantum Matter, Beijing 100871, China
[3] Center for High Energy Physics, Peking University, Beijing 100871, China
[4] Amherst Center for Fundamental Interactions, Department of Physics, University of Massachusetts-Amherst, Amherst, MA 01003, U.S.A.

Abstract: We investigate new physics effects on the Wtb effective couplings in a model-independent framework. The new physics effects can be parametrized by four independent couplings, f_1^L, f_1^R, f_2^L and f_2^R. We further introduce a set of parameters x_0, x_m, x_p and x_5 which exhibit a linear relation to the single top production cross sections. Using recent data for the t-channel single top production cross section σ_t, tW associated production cross section $\sigma_{\rm tW}$, s-channel single top production cross section σ_s, and W-helicity fractions F_0, F_L and F_R collected at the 8 TeV LHC and Tevatron, we perform a global fit to impose constraints on the top quark effective couplings. Our global fitting results show that the top quark effective couplings are strongly correlated. We show that (i) improving the measurements of σ_t and $\sigma_{\rm tW}$ is important in constraining the correlation of (f_1^R, f_2^R) and (f_2^L, f_2^R); (ii) f_1^L and f_2^R are anti-correlated, and are sensitive to all the four experiments; (iii) f_1^R and f_2^L are also anti-correlated, and are sensitive to the F_0 and F_L measurements; (iv) the correlation between f_2^L and f_2^R is sensitive to the precision of the σ_t, $\sigma_{\rm tW}$ and F_0 measurements. The effective Wtb couplings are studied in three kinds of new physics models: the $G(221) = SU(2)_1 \otimes SU(2)_2 \otimes U(1)_X$ models, the vector-like quark models and the Littlest Higgs model with and without T-parity. We show that the Wtb couplings in the left-right model and the un-unified model are sensitive to the ratio of gauge couplings when the new heavy gauge boson's mass ($M_{\rm W'}$) is less than several hundred GeV, but the constraint is loose if $M_{\rm W'} > 1$ TeV. Furthermore, the Wtb couplings in vector-like quark models and the Littlest Higgs models are sensitive to the mixing angles of new heavy particles and SM particles.

Keywords: top quark, TeV physics, anomalous coupling

PACS: 14.65.Ha **DOI:** 10.1088/1674-1137/41/6/063101

1 Introduction

The discovery of the Higgs boson at the Large Hadron Collider (LHC) [1, 2] completes the Standard Model (SM) of particle physics. So far, no evidence of new physics (NP) has been observed at the LHC. It is possible that the scale of new physics $\Lambda_{\rm NP}$ is much higher than the electroweak symmetry breaking (EWSB) scale ($v = 246$ GeV). If so, we expect to look for indirect effects of NP with the SM particles which we know. The top quark, discovered at the Tevatron [3, 4], is the heaviest particle in the SM. With its mass around the EWSB scale, the top quark is believed to play an important role in connecting the SM and NP. The Wtb coupling plays a pivotal role in top quark physics. The top quark decay and single top quark production processes are sensitive to the Wtb coupling. In addition, it offers a very promising way to probe for NP at the LHC. For instance, the production rate of single top quarks and the polarization of the top quark can be modified by NP beyond the SM, such as new gauge boson W′s, vector-like fermions, etc. Those heavy particles are predicted in many NP models, such as $SU(2)_1 \otimes SU(2)_2 \otimes U(1)_X$, often denoted as $G(221)$ models [5, 6], vector-like quark models [7–10], Little Higgs models [11–13], warped/composite simpli-

Received 23 January 2017

∗ Supported by National Science Foundation of China (11275009, 11675002, 11635001), National Science Foundation (PHY-1315983, PHY-1316033) and DOE (DE- SC0011095)

1) E-mail: qinghongcao@pku.edu.cn

2) E-mail: binyan@pku.edu.cn

3) E-mail: jhyu@physics.umass.edu

4) E-mail: larry@pku.edu.cn

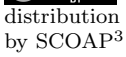

fied models [14] and many others. It is convenient to classify the underlying theories according to different approaches that modify the Wtb coupling. A simple case is that the new heavy particles mix with SM particles at tree-level, like a new gauge boson W′ or a new fermion T(B). Another way to generate the anomalous Wtb coupling is through the loop-level. Typical examples are supersymmetric models [15, 16] and two-Higgs-doublet models [17].

The top quark decays before hadronization as its lifetime is much smaller than the typical hadronization time scale. In the SM, the dominant decay mode of top quark is $t \to W^+b$, so the Wtb coupling governs the top quark decay process. One way to probe the structure of the Wtb coupling is to study the helicity fractions of the W boson in top quark decay. The W-boson helicity fractions are defined as the partial rate for a given helicity state divided by the total decay rate: $F_{L,R,0} \equiv \Gamma_{L,R,0}/\Gamma$, where F_L, F_R, F_0 are the left-handed, right-handed and longitudinal helicity fractions, respectively. The W helicity fractions, calculated to the accuracy of the next-to-next-to-leading order (NNLO) QCD corrections in the SM, are $F_0 = 0.687\pm0.005$, $F_L = 0.311\pm0.005$, $F_R = 0.0017\pm0.0001$ for a top quark mass of $m_t = 172.8 \pm 1.3$ GeV [18, 19]. Recently, the ATLAS and CMS collaborations have measured the W helicity fractions in top quark decays at $\sqrt{s}$ = 7 TeV, and CMS 8 TeV results are also available. These results are consistent with the SM predictions [19, 20].

At hadron colliders, the top quark can be produced singly in three channels: the t-channel process ($ub \to td$), the tW associated production process ($bg \to tW^-$), and the s-channel process ($u\bar{d} \to W^+ \to t\bar{b}$). The t-channel cross section is predicted at next-to-next-to-leading order plus the contribution due to the resummation of soft-gluon bremsstrahlung (NNLO+NNLL) to be $\sigma_t = 87.8^{+3.4}_{-1.9}$ pb [21, 22] at the LHC with $\sqrt{s} = 8$ TeV. The theoretical predictions for the tW-channel and s-channel at $\sqrt{s} = 8$ TeV at NLO+NNLL precision in QCD are $\sigma_{Wt} = 22.4 \pm 1.5$ pb [23] and $\sigma_s = 5.6 \pm 0.2$ pb [24], respectively. The cross sections at $\sqrt{s} = 13$ TeV are $\sigma_t = 221^{+6}_{-2} \pm 3$ pb, $\sigma_{Wt} = 72.6 \pm 1.3 \pm 1.3$ pb and $\sigma_s = 11.29 \pm 0.18 \pm 0.26$ pb [25]. Recently, both ATLAS and CMS collaborations have measured the single top quark production cross sections at $\sqrt{s} = 7$ TeV, $\sqrt{s} = 8$ TeV and $\sqrt{s} = 13$ TeV. These are summarized in Sec. 3.

In this work, we use the effective field theory (EFT) to calculate the single top quark production cross sections and W helicity fractions, and use the recent experimental data (denoted as Wtb measurements) to determine the general Wtb couplings. Model independent analyses of the Wtb couplings have already been performed using the EFT approach, see for example in Refs. [26–49]. In our work, we compute the deviation from the SM by including the dimension-6 operators for top quark decay and single top quark production processes. We incorporate the quadratic terms of dimension-6 operators to obtain the correlations among different operators in the single top quark cross section and W helicity fraction calculations. The constraints on Wtb couplings based on some of the recent experimental data were studied in Refs. [46, 47]. We perform a global fit of the general Wtb couplings by analysing the correlations among different couplings and discuss the implication of the top quark effective theory for several NP models.

The paper is organized as follows. In Section 2 we calculate the single top quark production cross sections via an effective field theory approach. In Section 3 we present the allowed parameter space of the general Wtb couplings after incorporating the most recent ATLAS and CMS results. In Section 4 we discuss the constraints on various new physics models from the Wtb couplings. Finally, we conclude in Section 5.

2 Top quark effective field theory

2.1 Dimension-6 operators and effective Wtb couplings

Using the EFT approach to explore possible NP effects has been discussed widely, see for example Refs. [27, 29, 30, 32, 40, 50–57]. A model-independent way to parametrize the low energy effects of NP theories is the linearly realized effective Lagrangian, which incorporates the particle content and symmetries of the SM. The nonlinearly realized mechanism of the electroweak symmetry is studied in Refs. [27, 51, 53, 54]. In this paper, we assume the new scalar particle observed at the LHC is the SM Higgs boson, and use the linear realization to parametrize the NP effects [50, 55]. The effective Lagrangian before electroweak symmetry breaking is

$$\mathcal{L}_{\rm eff} = \mathcal{L}_{\rm SM} + \sum_i \frac{C_i}{\Lambda^2} O_i + \mathcal{O}\left(\frac{1}{\Lambda^3}\right), \tag{1}$$

where $\mathcal{L}_{\rm SM}$ is the SM Lagrangian, Λ is the characteristic scale of new physics, O_i denotes $SU(3)_c \otimes SU(2)_L \otimes U(1)_Y$ gauge invariant dimension-6 operators, and C_i corresponds to the Wilson coefficient which represents the strength of the effective operator O_i. The dimension-5 operator violates lepton number conservation and is not considered in this work. The close agreement between experimental measurements and SM predictions indicates that the NP effects should be small. Hence, we restrict ourselves to dimension-6 operators in this work. The complete set of dimension-6 effective operators generating anomalous Wtb couplings is [50, 55]

$$O^{(3)}_{\phi q} = {\rm i}(\phi^\dagger \tau^I D_\mu \phi)(\bar{q}_L \gamma^\mu \tau^I q_L), \quad O_{\phi\phi} = {\rm i}(\tilde{\phi}^\dagger D_\mu \phi)(\bar{t}_R \gamma^\mu b_R),$$

$$O_{Dt}=(\bar{q}_L D_\mu t_R)D^\mu\tilde{\phi}, \quad O_{\bar{D}t}=(D_\mu\bar{q}_L t_R)D^\mu\tilde{\phi}, \quad O_{tW}=(\bar{q}_L\sigma^{\mu\nu}\tau^I t_R)\tilde{\phi}W^I_{\mu\nu}, \quad O_{bW}=(\bar{q}_L\sigma^{\mu\nu}\tau^I b_R)\phi W^I_{\mu\nu},$$
$$O_{Db}=(\bar{q}_L D_\mu b_R)D^\mu\phi, \quad O_{\bar{D}b}=(D_\mu\bar{q}_L b_R)D^\mu\phi, \quad O_{qW}=\bar{q}_L\gamma^\mu\tau^I D^\nu q_L W^I_{\mu\nu}. \tag{2}$$

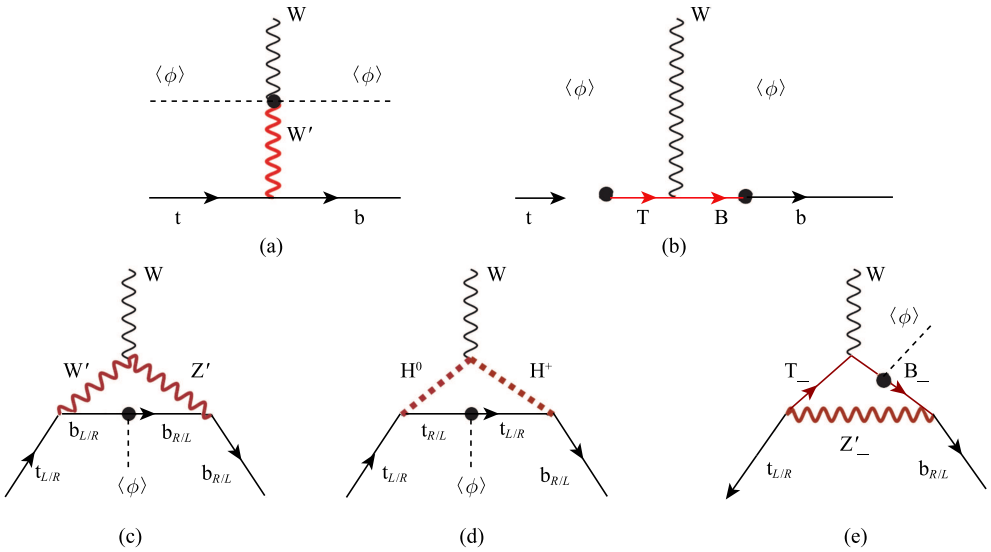

Fig. 1. Relations between effective operators and NP models. (a) and (b) show the tree level mixing effect between the new heavy particles and SM particles; (c)–(e) show the possible loop-induced dimension-6 operator diagrams of some extension NP models.

where $q_L^T=(t,b)_L$ denotes the $SU(2)_L$ weak doublet of the third generation left-handed quark fields, t_R and b_R are $SU(2)_L$ weak singlets of right-handed top and bottom-quark fields respectively, ϕ is a $SU(2)_L$ weak doublet of the Higgs field, defined $\phi^T=\frac{1}{\sqrt{2}}(0,v+h)$ with $v=246$ GeV in the unitarity gauge with $\tilde{\phi}=\mathrm{i}\tau^2\phi^*$, and $D_\mu=\partial_\mu-\mathrm{i}g(\tau^I/2)W^I_\mu-\mathrm{i}g'B_\mu Y$ is the covariant derivative, where g and g' are gauge couplings of $SU(2)_L$ and $U(1)_Y$, respectively, and Y is the hypercharge of the field to which D_μ is applied. $W^I_{\mu\nu}=\partial_\mu W^I_\nu-\partial_\nu W^I_\mu+g\varepsilon_{IJK}W^J_\mu W^K_\nu$ are the strength tensors of the $SU(2)_L$ gauge fields, ε_{IJK} denotes the structure constants, and τ^I is the usual Pauli matrix.

Three types of dimension-6 operators contribute to the Wtb couplings. The first type is operators involving a scalar field carrying one covariant derivative, the second is operators involving fermion and scalar fields both carrying one covariant derivative, and the third is operators involving field strength tensors.

The operators $O^{(3)}_{\phi q}$ and $O_{\phi\phi}$ are of the first type. They can be generated at tree-level after integrating out the new heavy particles, such as a heavy charged vector boson ($\mathrm{W}'^{\pm}$) that mixes with SM gauge boson $\mathrm{W}^{\pm}$ [5, 6] or a heavy quark that mixes with top quark or bottom quark [9, 10]. A pictorial illustration of the relation between the tree-level effective operators and the possible NP models is shown in Fig. 1(a) and Fig. 1(b). We use the bold-red line to denote the NP particles. The anomalous Wtb couplings arise at tree-level after spontaneous symmetry breaking with $\langle\phi\rangle=v/\sqrt{2}$.

The operators O_{Dt}, $O_{\bar{\mathrm{D}}\mathrm{t}}$, O_{Db}, $O_{\bar{\mathrm{D}}\mathrm{b}}$ fall into the second category. Those operators give a contribution of order p^2/Λ^2, where p is the typical momentum scale in the process. Such operators, corresponding to the vertices involving three external lines, can be induced only at loop-level after integrating out the heavy particles [58].

The operators O_{tW}, O_{bW}, O_{qW} are of the third type. Usually, effective operators which involve the field strength tensor are generated only at loop level if the complete theory is a gauge theory [58]. Typical examples include supersymmetric models [15, 16, 59], two-Higgs-doublet models [17], etc.

A pictorial illustration of the relation between loop-induced effective operators and the possible underlying theories is shown in Fig. 1(c–e). The Wtb coupling can be induced in the NP models with extended gauge structure, which yields extra gauge bosons (see Fig. 1(c)), or new scalar particles which consist of a new charge scalar and neutral scalar (see Fig. 1(d)), or new fermions which carry one discrete quantum number to avoid mixing with the top quark and bottom quark at tree-level (see Fig. 1(e)). We will comment on the impact of Wtb measurements on several NP models in Section 4.

As usual, the effective Lagrangians consist of redundant terms, which can be removed by the classical equations of motion [60]. This is based on the equivalence theorem of the S matrix. After we use the equations of motion to remove redundant operators, the relevant operators reduce to

$$\begin{aligned} O_{\phi q}^{(3)} &= \mathrm{i}(\phi^\dagger \tau^I D_\mu \phi)(\bar{q}_L \gamma^\mu \tau^I q_L) \\ O_{\phi\phi} &= \mathrm{i}(\tilde{\phi}^\dagger D_\mu \phi)(\bar{t}_R \gamma^\mu b_R), \\ O_{tW} &= (\bar{q}_L \sigma^{\mu\nu} \tau^I t_R)\tilde{\phi} W^I_{\mu\nu}, \\ O_{bW} &= (\bar{q}_L \sigma^{\mu\nu} \tau^I b_R)\phi W^I_{\mu\nu}. \end{aligned} \tag{3}$$

Assuming new anomalous couplings arise from the above dimension-6 operators, we can parametrize the general effective Wtb couplings as [36]

$$\begin{aligned} \mathcal{L}_{\mathrm{Wtb}} = &\frac{g}{\sqrt{2}} W^-_\mu \bar{b}\gamma^\mu \left((1+f_1^L)P_L + f_1^R P_R\right) t \\ &- \frac{g}{\sqrt{2} m_{\mathrm{W}}} \partial_\nu W^-_\mu \bar{b}\sigma^{\mu\nu}\left(f_2^L P_L + f_2^R P_R\right) t + \mathrm{h.c.}, \end{aligned} \tag{4}$$

where $P_{L,R} = (1 \mp \gamma_5)/2$ are the usual chirality projectors, m_{W} is the W-boson mass and the Cabibbo-Kobayaski-Maskawa matrix element V_{tb} is taken to be 1 in our analysis. In the SM, the values of the coefficients f_i vanish at tree-level. Those couplings could be generated if NP exists. Although those couplings can in general be complex quantities, we assume the four coefficients are real in our calculation[1)]. The coefficients of the effective Wtb couplings are related to the Wilson coefficients of the dimension-6 operators as follows [29]:

$$\begin{aligned} f_1^L &= \frac{C_{\phi q}^{(3)*} v^2}{\Lambda^2}, & f_1^R &= \frac{1}{2} C^*_{\phi\phi} \frac{v^2}{\Lambda^2}, \\ f_2^L &= \sqrt{2} C^*_{\mathrm{bW}} \frac{v^2}{\Lambda^2}, & f_2^R &= \sqrt{2} C_{\mathrm{tW}} \frac{v^2}{\Lambda^2}. \end{aligned} \tag{5}$$

2.2 Single top production

In this section we discuss the contribution of general effective Wtb couplings to the total cross sections of single top production and the W helicity fractions in top quark decay. In this work, we focus on the four independent operators, see Eq. (3). The top quark can be produced singly through the electroweak interaction. Depending on the kinematics of the W boson involved, single top production is usually sub-categorized into three channels: s-channel production ($q^2_{\mathrm{W}} > 0$), t-channel production ($q^2_{\mathrm{W}} < 0$), and tW associated production ($q^2_{\mathrm{W}} = m^2_{\mathrm{W}}$), where q_{W} denotes the four momentum of the W boson.

We separate the total cross section of the single top production into the SM contribution plus the contributions from anomalous Wtb couplings

$$\sigma_i = \sigma_i^{\mathrm{SM}} + K\Delta\sigma_i, \tag{6}$$

where σ_i^{SM} denotes the cross section of the i-channel ($i = s, t, \mathrm{tW}$) single top production in the SM with the approximate NNLO QCD correction, and $\Delta\sigma_i$ denotes the variation from the SM prediction induced by the anomalous couplings at tree level. The K-factor, defined as $K \equiv \sigma^{\mathrm{SM}}_{\mathrm{NNLO}}/\sigma^{\mathrm{SM}}_{\mathrm{LO}}$, describes the approximate NNLO QCD corrections in the SM. We assume the anomalous couplings receive exactly the same corrections as the SM processes. Following Ref. [36] we write the contributions of anomalous couplings to the single top productions as

$$\begin{aligned} \Delta\sigma_t &= a_0 x_0 + a_m x_m + a_p x_p + a_5 x_5, \\ \Delta\sigma_s &= b_0 x_0 + b_m x_m + b_p x_p + b_5 x_5, \\ \Delta\sigma_{\mathrm{tW}} &= c_0 x_0 + c_m x_m + c_p x_p + c_5 x_5, \end{aligned} \tag{7}$$

where we reparametrize the four coefficients $f_{1,2}^{L,R}$ as x_0, x_m, x_p, x_5 [36]

$$\begin{aligned} x_0 &= \left(1 + f_1^L + \frac{f_2^R}{a_t}\right)^2 + \left(f_1^R + \frac{f_2^L}{a_t}\right)^2 - 1, \\ x_m &= \left(1 + f_1^L + a_t f_2^R\right)^2 - 1, \\ x_p &= \left(f_1^R + a_t f_2^L\right)^2, \\ x_5 &= a_t^2\left[(f_2^L)^2 + (f_2^R)^2\right], \end{aligned} \tag{8}$$

with $a_t \equiv m_{\mathrm{t}}/m_{\mathrm{W}}$. Note that the terms proportional to the bottom quark mass have been ignored in our calculation due to the suppression factor $(m_{\mathrm{b}}/m_{\mathrm{W}})^2$ [2)].

The coefficients (a_i, b_i and c_i) depend on the collider type and energy and have to be calculated numerically. Ref. [36] calculated the a_i's and b_i's at the Tevatron Run II and 14 TeV LHC. In this work we update both the a_i's and b_i's using the CTEQ6L parton distribution functions (PDFs) [62] at the 7 TeV, 8 TeV and 13 TeV LHC. The numerical values of the coefficients are shown in Table 1.

1) The complex anomalous couplings have been studied in Ref. [47], and the ATLAS collaboration also give a constraint on the imaginary part of f_2^R in Ref. [61].

2) We deem that neglecting the bottom quark mass in the present work is reasonable because inclusion of the bottom mass only induces a tiny asymmetry of about $0.01 \sim 0.02$ [46, 47] in the allowed region of $f_{1,2}^{L,R}$, whereas the length of the marginal allowed region of one variable in the global fit is typically $\mathcal{O}(1)$, see Fig. 2. Even if only one parameter such as f_1^R is allowed to vary and all the other parameters are turned off, the length of the allowed region reaches about 0.2 (see Fig. 5) which is still larger than the amount of asymmetry induced by the bottom mass.

Table 1. The coefficients a_i, b_i and c_i in Eq. (7) for single top quark production. All the coefficients are in units of picobarns. The SM cross section at the approximate NNLO with $m_t = 173$ GeV (σ_i^{SM} where $i = \{t, s, \mathrm{tW}\}$ channels) and the K_i factors [24, 25, 63–74] are also shown.

t-channel	a_0	a_m	a_p	a_5	$\sigma_t^{\rm SM}$	K
LHC (7 TeV t)	42.355	−4.290	−9.700	17.514	43.0	1.13
LHC (7 TeV $\bar{\rm t}$)	24.251	−5.315	−2.514	9.748	22.9	1.21
LHC (8 TeV t)	56.060	−5.990	−12.727	23.582	56.4	1.13
LHC (8 TeV $\bar{\rm t}$)	32.846	−7.139	−3.594	13.423	30.7	1.19
LHC (13 TeV t)	142.763	−17.718	−31.487	63.636	138.0	1.10
LHC (13 TeV $\bar{\rm t}$)	90.369	−19.136	−11.450	39.062	83.0	1.16
s-channel	b_0	b_m	b_p	b_5	$\sigma_s^{\rm SM}$	K
Tevatron (t/$\bar{\rm t}$)	−0.099	0.419	0.419	0.281	0.523	1.68
LHC (8 TeV t)	−0.724	2.917	2.917	2.873	3.79	1.73
LHC (8 TeV $\bar{\rm t}$)	−0.384	1.584	1.584	1.364	1.76	1.47
tW channel	c_0	c_m	c_p	c_5	$\sigma_{tW}^{\rm SM}$	K
LHC (7 TeV t/$\bar{\rm t}$)	7.592	−2.777	−2.777	5.386	7.8	1.62
LHC (8 TeV t/$\bar{\rm t}$)	11.095	−4.055	−4.055	7.990	11.1	1.58
LHC (13 TeV t/$\bar{\rm t}$)	38.622	−14.076	−14.076	29.339	36.3	1.48

To obtain the coefficients (c_0, c_m, c_p, c_5) of the tW-channel single top production, we rewrite the cross section in terms of different combinations of the effective couplings

$$\begin{aligned}\Delta\sigma_{\rm tW} = &\left[(1+f_1^L)^2-1+(f_1^R)^2\right]\sigma_0+\left[(1+f_1^L)f_2^R\right.\\&\left.+f_1^R f_2^L\right]\sigma_{N1}+\left[(f_2^L)^2+(f_2^R)^2\right]\sigma_{N2},\end{aligned}\tag{9}$$

where σ_0 denotes the SM LO prediction while σ_{N1} and σ_{N2} represent the partial cross section that is proportional to f_2^R and $(f_2^R)^2$, respectively. The cross sections σ_0, σ_{N1} and σ_{N2} are obtained by integrating out the final state phase space, and then convoluting with the initial state PDFs. The coefficients (c_0, c_m, c_p, c_5) are then determined from σ_0, σ_{N1} and σ_{N2} as follows:

$$\begin{aligned}&c_0 = \frac{\sigma_{N1}a_t - 2\sigma_0 a_t^2}{2(1-a_t^2)}, \qquad c_m = \frac{2\sigma_0 - \sigma_{N1}a_t}{2(1-a_t^2)},\\&c_p = \frac{2\sigma_0 - \sigma_{N1}a_t}{2(1-a_t^2)}, \qquad c_5 = \frac{\sigma_{N2}}{a_t^2} - \frac{\sigma_{N1}-2\sigma_0 a_t}{2(1-a_t^2)a_t^3}\\&\quad - \frac{2\sigma_0 - \sigma_{N1}a_t}{2(1-a_t^2)}.\end{aligned}\tag{10}$$

The numerical values of the coefficients are given in Table 1 at the 7 TeV, 8 TeV and 13 TeV LHC.

With the help of the coefficients a_i, b_i and c_i, the contributions of the Wtb anomalous couplings can be written as:

$$\begin{aligned}\Delta\sigma_\beta = &2\Big(\beta_0+\beta_m\Big)f_1^L + 2\left(\frac{1}{a_t}\beta_0 + a_t\beta_m\right)f_2^R\\&+\Big(\beta_0+\beta_m\Big)\left(f_1^L\right)^2+\Big(\beta_0+\beta_p\Big)\left(f_1^R\right)^2\\&+2\left(\frac{1}{a_t}\beta_0+a_t\beta_m\right)f_1^L f_2^R + 2\left(\frac{1}{a_t}\beta_0+a_t\beta_p\right)f_1^R f_2^L\\&+\left(\frac{1}{a_t^2}\beta_0 + a_t^2\Big[\beta_p+\beta_5\Big]\right)\left(f_2^L\right)^2\\&+\left(\frac{1}{a_t^2}\beta_0 + a_t^2\Big[\beta_m+\beta_5\Big]\right)\left(f_2^R\right)^2,\end{aligned}\tag{11}$$

where $\beta_i = a_i, b_i, c_i$ denote the single top quark cross section coefficients of different channels.

2.3 W helicity fractions in top decay

For completeness, we also list the fractions of the W helicity in the top quark decay in terms of x_i [36],

$$\begin{aligned}F_0 &= \frac{a_t^2(1+x_0)}{a_t^2(1+x_0)+2(1+x_m+x_p)},\\F_L &= \frac{2(1+x_m)}{a_t^2(1+x_0)+2(1+x_m+x_p)},\\F_R &= \frac{2x_p}{a_t^2(1+x_0)+2(1+x_m+x_p)},\end{aligned}\tag{12}$$

where F_0, F_L and F_R represent the fractions of W bosons with longitudinal polarization (W_0), left-handed polarization (W_L) and right-handed polarization (W_R). x_0 represents the contribution from the W boson longitudinal polarization, and x_m and x_p denote the contributions from W boson left and right handed polarization, respectively.

Neglecting terms which are proportional to the bottom quark mass, the tree level results of the W helicity

fractions in the SM are

$$F_0^{\rm SM}=\frac{a_t^2}{a_t^2+2}=0.70,\quad F_L^{\rm SM}=\frac{2}{a_t^2+2}=0.30,$$
$$F_R^{\rm SM}=0. \tag{13}$$

In the SM the top quark decays predominantly into the longitudinal W boson because the coupling of the top quark to the longitudinal W boson is similar to the Yukawa coupling, which is proportional to the top quark mass. The top quark cannot decay into a right-handed W boson owing to the purely left-handed Wtb coupling in the SM. When the bottom quark mass is ignored, the right-handed W boson is forbidden by angular momentum conservation.

However, the anomalous coupling f_1^R or f_2^L can yield a right-handed W boson in top quark decay. Different from the f_1^R coupling, the f_2^L contribution to a W_R involves flipping the chirality of the top quark, which gives rise to a factor of a_t. Therefore, F_R is proportional to $x_p=(f_1^R+a_tf_2^L)^2$. Similarly, the f_2^R coupling can also produce a W_L in the top quark decay by flipping the top quark's chirality. As a result, F_L is proportional to $1+x_m=(1+f_1^L+a_tf_2^R)^2$. All of the four effective Wtb couplings can generate a W_0 in the top quark decay. F_0 is proportional to $a_t^2(1+x_0)=(a_t+a_tf_1^L+f_2^R)^2+(a_tf_1^R+f_2^L)^2$.

3 Global fit of the effective Wtb couplings

3.1 Experimental data and statistical analysis

The single top production cross sections and the W helicity fractions have been measured at the Tevatron and the LHC. The best measurement of the cross section of the s-channel single-top production is given at the Tevatron at $\sqrt{s}=1.96$ TeV with luminosity 9.7 fb^{-1} [75]. We also consider the updated experimental results of the t-channel and tW-channel cross sections and W-helicity measurements at both the CMS and ATLAS collaborations. All the experimental data are summarized in Table 2.

Table 2. Recent measurements of the cross sections for the single top quark productions and the W helicity fractions at the Tevatron and LHC.

	CMS	ATLAS	Tevatron
s-channel (1.96 TeV)	–	–	$1.29^{+0.26}_{-0.24}$ pb [75]
s-channel (8 TeV)	–	$4.8\pm1.1^{+2.2}_{-2.0}$ pb [76] (value± stat± sys)	-
t-channel (8 TeV)	$83.6\pm2.3\pm7.4$ pb [77] (value± stat± sys)	$82.6\pm1.2\pm11.4\pm3.1\pm2.3$ pb [78] (value± stat± syst± PDF± lumi)	–
t-channel (13 TeV)	$227.9\pm9.1\pm14.0^{+28.7}_{-27.7}\pm3.8$ pb [79] (value± stat± sys± exp± theo± lumi)	$247\pm6.4\pm32.5\pm3.1\pm3.6$ pb [80] (value± stat± syst± PDF± lumi)	–
tW-channel (8 TeV)	25.0 ± 4.7 pb [81]		–
tW-channel (13 TeV)	–	94 ± 10 (stat.)$^{+28}_{-23}$ (syst.) pb [82]	–
W-helicity (7 TeV)	$F_0=0.626\pm0.034$(stat.)±0.048(syst.) $F_L=0.359\pm0.021$(stat.)±0.028(syst.)[20] $F_R=0.015\pm0.034$		–
W-helicity (8 TeV)	$F_0=0.659\pm0.015$(stat.)±0.023(syst.) $F_L=0.350\pm0.010$(stat.)±0.024(syst.)[19] $F_R=-0.009\pm0.006$(stat.)±0.020(syst.)	–	–

We perform a global χ^2 test to obtain the present constraints on the effective Wtb couplings. In the statistical analysis, the χ^2 is defined as

$$\chi^2=\sum_i\frac{(\mathcal{O}_i^{\rm exp}-\mathcal{O}_i^{\rm th})^2}{\delta\sigma_i^2}, \tag{14}$$

where $\mathcal{O}_i^{\rm exp}$ and $\mathcal{O}_i^{\rm th}$ are the experimental values and the theoretical predictions for the experimental observable i, respectively. $\delta\sigma_i$ represents the total error of the experimental measurement, which is defined as $\delta\sigma_i\equiv\sqrt{(\delta\sigma_i^{\rm stat.})^2+(\delta\sigma_i^{\rm syst.})^2}$. The CERN library MINUIT [83] is used in our analysis to obtain the best-fit values of the effective Wtb couplings and the contours at different confidence levels (C.L.).

In this work we consider both direct and indirect constraints on the effective Wtb couplings. The direct constraints arise from the experimental measurements of top quark productions and decays, while the indirect constraints arise from precision measurements of flavor physics. For example, the anomalous Wtb cou-

plings can contribute to flavor changing neutral current (FCNC) processes through quantum effects involving top quarks inside the loop. In particular, the inclusive decay $\bar{B} \to X_s\gamma$ provides very stringent bounds on the anomalous Wtb couplings [84].

3.2 Constraints on the effective couplings and operators

Below we present the allowed regions of the effective Wtb couplings based on a global-fit analysis of all the four effective Wtb couplings $f_{1,2}^{L,R}$. We plot in Fig. 2 the allowed parameter space for the effective Wtb couplings at 68%, 90% and 95% C.L., and investigate the correlations among the effective Wtb couplings. We note that the allowed parameter space on the plane of the (f_1^L, f_1^R) and (f_1^L, f_2^L) contours is mainly driven by the t-channel and tW-channel cross sections. Figure 2(a) shows the allowed parameter space of (f_1^L, f_1^R). The cross sections of the single top quark production processes are proportional to $(1+f_1^L)^2$ and $(f_1^R)^2$; see Eq. (11). It yields a circular contour region on the plane of f_1^L and f_1^R and favors a negative f_1^L. Figure 2(b) displays the contour on the plane of (f_1^L, f_2^L), which is elliptical. Even though the cross sections are proportional to $(1+f_1^L)^2$ and $(f_2^L)^2$, the $(f_2^L)^2$ term contributes less to the cross section than the $(1+f_1^L)^2$ term. This generates the ellipse shape. We also note that the differences among the parameter spaces at the three confidence levels are very small. This is because the contours of the effective couplings on the plane of two effective Wtb couplings are a projection from the four dimension parameter space down to a two dimension subspace. That projection leads to the small differences.

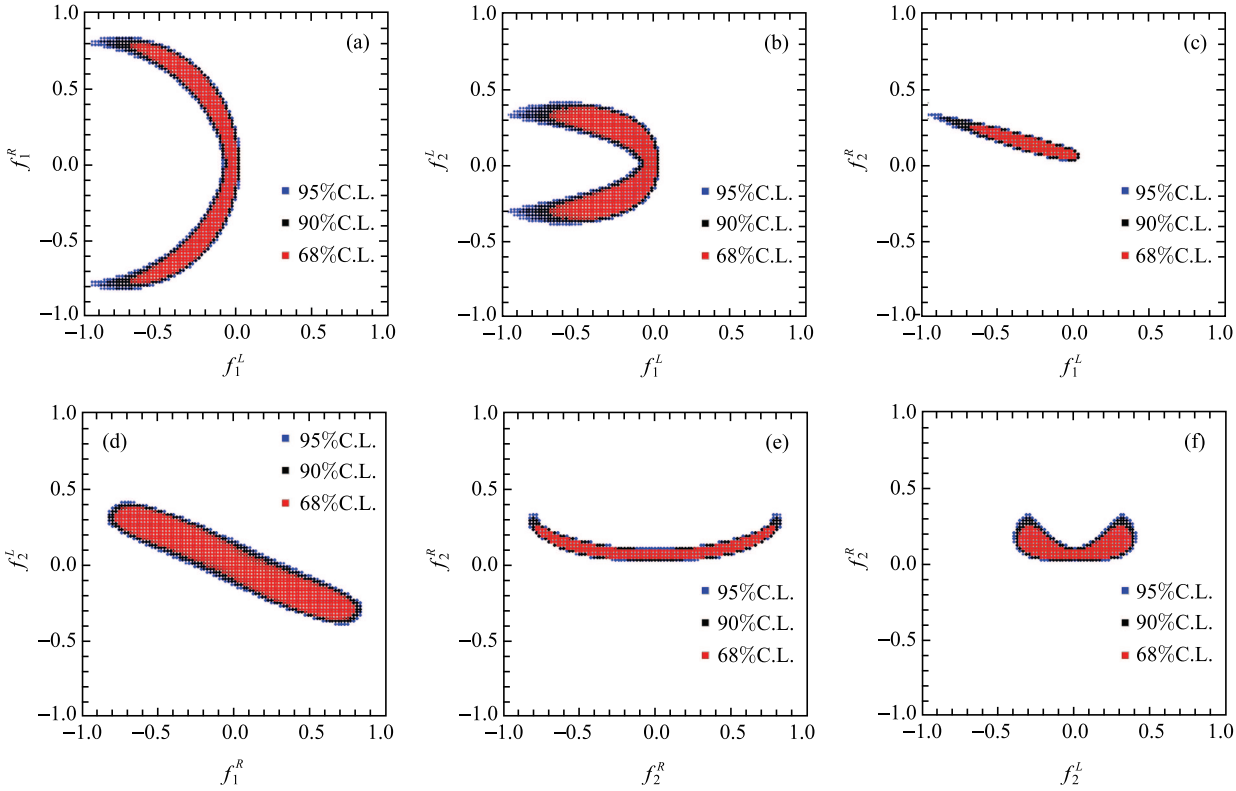

Fig. 2. (color online) Allowed parameter space on the plane of the effective Wtb couplings at confidence levels of 68% (red region), 90% (black region) and 95% (blue region). $|f_1^L| \leqslant 1$ is required in our analysis.

The (f_1^L, f_2^R) contour shown in Fig. 2(c) clearly indicates a strong anti-correlation between f_1^L and f_2^R. Such a behavior can be understood from the single top production cross sections, which are approximately proportional to $(1+f_1^L+a_t f_2^R)^2$. As a result, the two islands of the allowed parameter space are symmetric around the point $(f_1^L=-1, f_2^R=0)$. Note that the region of $f_1^L<-1$ is also possible. The correlation in the (f_1^R, f_2^L) contour originates from the relation $(f_1^R + a_t f_2^L)^2$ in the cross sections, yielding the anti-correlation band in Fig. 2(d) which is centered around the point $(f_1^R=0, f_2^L=0)$. The tightest constraints on both the (f_1^L, f_2^R) and (f_1^R, f_2^L)

contours come from the tW-channel cross section and the W helicity fractions.

Figure 2(c) shows a positive f_2^R is preferred when demanding $|f_1^L| \leqslant 1$. Therefore, both the (f_1^R, f_2^R) and (f_2^L, f_2^R) contours only allow positive f_2^R. Due to the interference effect between the anomalous Wtb couplings and the SM, the linear term which is proportional to f_2^R is valid in the cross sections. Therefore the relation of f_2^R with f_1^R or f_2^L is like $f_2^R \sim a_1(f_1^R)^2$ or $b_1(f_2^L)^2$, as shown in Figs. 2(e) and (f). The tW channel cross section still determines the shapes of the (f_1^R, f_2^R) and (f_2^L, f_2^R) contours.

The current experimental data of σ_s and $\sigma_{\rm tW}$ exhibit $\sim 20\%$ uncertainties. The accuracy of $\sigma_{\rm tW}$ is expected to be improved at the forthcoming LHC Run 2 , but the precise measurement of σ_s is still challenging. We thus consider the σ_t, $\sigma_{\rm tW}$ and the W-helicity fractions in our global analysis to constrain the effective Wtb couplings. Using the x_i's while neglecting $O(x_i^2)$ and higher order contributions, we can extract the correlation between different channels:

$$\left(\begin{array}{cccc} a_0^{\rm tot}/\sigma_t^{\rm SM} & a_m^{\rm tot}/\sigma_t^{\rm SM} & a_p^{\rm tot}/\sigma_t^{\rm SM} & a_5^{\rm tot}/\sigma_t^{\rm SM} \\ c_0^{\rm tot}/\sigma_{\rm tW}^{\rm SM} & c_m^{\rm tot}/\sigma_{\rm tW}^{\rm SM} & c_p^{\rm tot}/\sigma_{\rm tW}^{\rm SM} & c_5^{\rm tot}/\sigma_{\rm tW}^{\rm SM} \\ F_L^{\rm SM} & -F_L^{\rm SM} & -F_L^{\rm SM} & 0 \\ -F_0^{\rm SM} & F_0^{\rm SM} & -F_L^{\rm SM} & 0 \end{array}\right)\left(\begin{array}{c} x_0 \\ x_m \\ x_p \\ x_5 \end{array}\right)$$

$$= \left(\begin{array}{c} \Delta\sigma_t^{\rm NP}/\sigma_t^{\rm SM} \\ \Delta\sigma_{\rm tW}^{\rm NP}/\sigma_{\rm tW}^{\rm SM} \\ \Delta F_0^{\rm NP}/F_0^{\rm SM} \\ \Delta F_L^{\rm NP}/F_L^{\rm SM} \end{array}\right), \tag{15}$$

where $\Delta\sigma_t^{\rm NP} \equiv (\sigma_t^{\rm exp} - \sigma_t^{\rm SM})$ and $\Delta\sigma_{\rm tW}^{\rm NP} \equiv (\sigma_{\rm tW}^{\rm exp} - \sigma_{\rm tW}^{\rm SM})$ are the variations from the SM prediction. $\Delta F_0^{\rm NP} \equiv (F_0^{\rm exp} - F_0^{\rm SM})$ and $\Delta F_L^{\rm NP} \equiv (F_L^{\rm exp} - F_L^{\rm SM})$ denote the variation of W_0 and W_L helicity fractions from the SM theory prediction. The factor $a_i^{\rm tot}$ and $c_i^{\rm tot}$ are given by:

$$a_i^{\rm tot} = K(t)\ a_i(t) + K(\bar{t})\ a_i(\bar{t}), \tag{16}$$

$$c_i^{\rm tot} = 2K({\rm tW})\ c_i({\rm tW}), \tag{17}$$

where the coefficients a_i and c_i are given in Table 1. $K(t)$ denotes the K-factor of the t-channel single top quark production, $K(\bar{\rm t})$ denotes the K-factor of the t-channel single anti-top quark production and the $K({\rm tW})$ is the K-factor of the tW associated production. Solving the systems of linear equations shown in Eq. 15 gives rise to the following relations

$$\left(\begin{array}{c} x_0 \\ x_m \\ x_p \\ x_5 \end{array}\right) = \left(\begin{array}{cccc} 1.756 & -0.755 & 0.267 & -0.068 \\ 1.756 & -0.755 & -0.733 & 0.932 \\ 0 & 0 & -2.315 & -1.000 \\ -1.547 & 1.545 & -1.918 & 0.060 \end{array}\right)$$

$$\cdot \left(\begin{array}{c} \sigma_t^{\rm exp(0)}/\sigma_t^{\rm SM} - 1 \\ \sigma_{\rm tW}^{\rm exp(0)}/\sigma_{\rm tW}^{\rm SM} - 1 \\ F_0^{\rm exp(0)}/F_0^{\rm SM} - 1 \\ F_L^{\rm exp(0)}/F_L^{\rm SM} - 1 \end{array}\right), \tag{18}$$

where $\sigma_t^{\rm exp(0)}$ and $\sigma_{\rm tW}^{\rm exp(0)}$ denote central values of the experimental data of t-channel and tW-channel cross sections, respectively. Similarly, $F_0^{\rm exp(0)}$ and $F_L^{\rm exp(0)}$ are experimental central values of the longitudinal and left-handed helicity fraction. Note that the central values of the experimental data determine the x_i's and the correlations of effective couplings, while the experimental errors are translated into the errors of x_i's (δx_i) which yield the allowed parameter spaces of those effective couplings. Below we employ the error propagation equation of the weighted sums functions to study the dependence of the δx_i's on experimental errors, which are labelled as $\delta\sigma_t^{\rm exp}$, $\delta\sigma_{\rm tW}^{\rm exp}$, $\delta F_0^{\rm exp}$ and $\delta F_L^{\rm exp}$.

The variance of x_0 is

$$(\delta x_0)^2 = 3.084\left(\frac{\delta\sigma_t^{\rm exp}}{\sigma_t^{\rm SM}}\right)^2 + 0.570\left(\frac{\delta\sigma_{\rm tW}^{\rm exp}}{\sigma_{tW}^{\rm SM}}\right)^2 + 0.071\left(\frac{\delta F_0^{\rm exp}}{F_0^{\rm SM}}\right)^2 + 0.005\left(\frac{\delta F_L^{\rm exp}}{F_L^{\rm SM}}\right)^2, \tag{19}$$

in which the σ_t and $\sigma_{\rm tW}$ measurements dominate over the W-helicity measurements. Improving the measurements of σ_t and $\sigma_{\rm tW}$ is important to test the correlations of (f_1^R, f_2^R) and (f_2^L, f_2^R).

The variance of x_m is

$$(\delta x_m)^2 = 3.084\left(\frac{\delta\sigma_t^{\rm exp}}{\sigma_t^{\rm SM}}\right)^2 + 0.570\left(\frac{\delta\sigma_{\rm tW}^{\rm exp}}{\sigma_{\rm tW}^{\rm SM}}\right)^2 + 0.537\left(\frac{\delta F_0^{\rm exp}}{F_0^{\rm SM}}\right)^2 + 0.869\left(\frac{\delta F_L^{\rm exp}}{F_L^{\rm SM}}\right)^2. \tag{20}$$

All coefficients are comparable, such that one has to consider all the four experiments to determine δx_m. As f_1^L and f_2^R are anti-correlated in $x_m = (1 + f_1^L + a_t f_2^R)^2 - 1$, improving δx_m would further constrain the correlation between f_1^L and f_2^R, i.e. the band in Fig. 2(c) tends to be narrower.

The $x_p = (f_1^R + a_t f_2^L)^2$ is directly linked to the right-handed W-helicity fraction F_R, which is inferred from F_L and F_0 measurements. As a result, δx_p depends only on the W-helicity measurement as following:

$$(\delta x_p)^2 = 5.359\left(\frac{\delta F_0^{\rm exp}}{F_0^{\rm SM}}\right)^2 + \left(\frac{\delta F_L^{\rm exp}}{F_L^{\rm SM}}\right)^2. \tag{21}$$

As a result, a strong anti-correlation between f_1^R and f_2^L can be obtained from the F_0 and F_L measurements.

The variance of x_5 is given by

$$(\delta x_5)^2 = 2.393\left(\frac{\delta\sigma_t^{\rm exp}}{\sigma_t^{\rm SM}}\right)^2 + 2.387\left(\frac{\delta\sigma_{\rm tW}^{\rm exp}}{\sigma_{\rm tW}^{\rm SM}}\right)^2 + 3.679\left(\frac{\delta F_0^{\rm exp}}{F_0^{\rm SM}}\right)^2 + 0.004\left(\frac{\delta F_L^{\rm exp}}{F_L^{\rm SM}}\right)^2. \quad (22)$$

It is sensitive to the precision of σ_t, $\sigma_{\rm tW}$ and F_0 measurements.

From the precision measurement of the Wtb couplings, one can also derive conservative bounds on the NP scales when no deviation is seen compared to SM predictions. Though we expect $C_i = O(1)$, their precise values are unknown. Measurements such as the ones described above can be used to obtain the ratios of these coefficients, but the values of Λ_i cannot be obtained separately. Therefore, we define dimensionless parameters $\widetilde{C}_i$ according to the Wilson coefficient C_i and normalize to 1 TeV,

$$\widetilde{C}_i \equiv C_i\left(\frac{1\ {\rm TeV}}{\Lambda}\right)^2. \quad (23)$$

The allowed parameter contours for the parameters $\widetilde{C}^{(3)}_{\phi q}$, $\widetilde{C}_{\phi\phi}$, $\widetilde{C}_{\rm bW}$, $\widetilde{C}_{\rm tW}$ are shown in Fig. 3. Although the values of effective couplings f_1^L, f_1^R, f_2^L and f_2^R are of the same order of magnitude, each individual parameter $\widetilde{C}_i$ is different. For example, the $\widetilde{C}_{\phi\phi}$ equal to 27 is also allowed at 95%C.L., while the maximal value for $\widetilde{C}_{\rm bW}$ and $\widetilde{C}_{\rm tW}$ is 5 at the same C.L. The difference comes from the relation between the effective couplings ($f_{1,2}^{L,R}$) and the Wilson coefficients C_i's in Eq. (5). In principle, after we know the range of the Wilson coefficients at low energy, we can obtain the values at NP scale Λ by renormalization group equations, and further determine the NP parameter space. However, in this paper, we focus on the model independent approach to search for NP effects, and will not calculate the mixing of the different operators.

Figure 4 displays the lower bound on the NP scale Λ_i obtained from the Wtb measurements at 95% C.L. with $|C_i| = 1$. The red bars represent those limits when all the four operators contribute simultaneously, while the blue bars display those limits obtained when we consider one parameter at a time. The current bound implies $\Lambda_{\phi q} > 246$ GeV, $\Lambda_{\phi\phi} > 188.6$ GeV, $\Lambda_{\rm bW} > 443.2$ GeV, $\Lambda_{\rm tW} > 561.7$ GeV when all the four operators contribute simultaneously, while $\Lambda_{\phi q} > 1000$ GeV, $\Lambda_{\phi\phi} > 440.6$ GeV when we consider one parameter at a time.

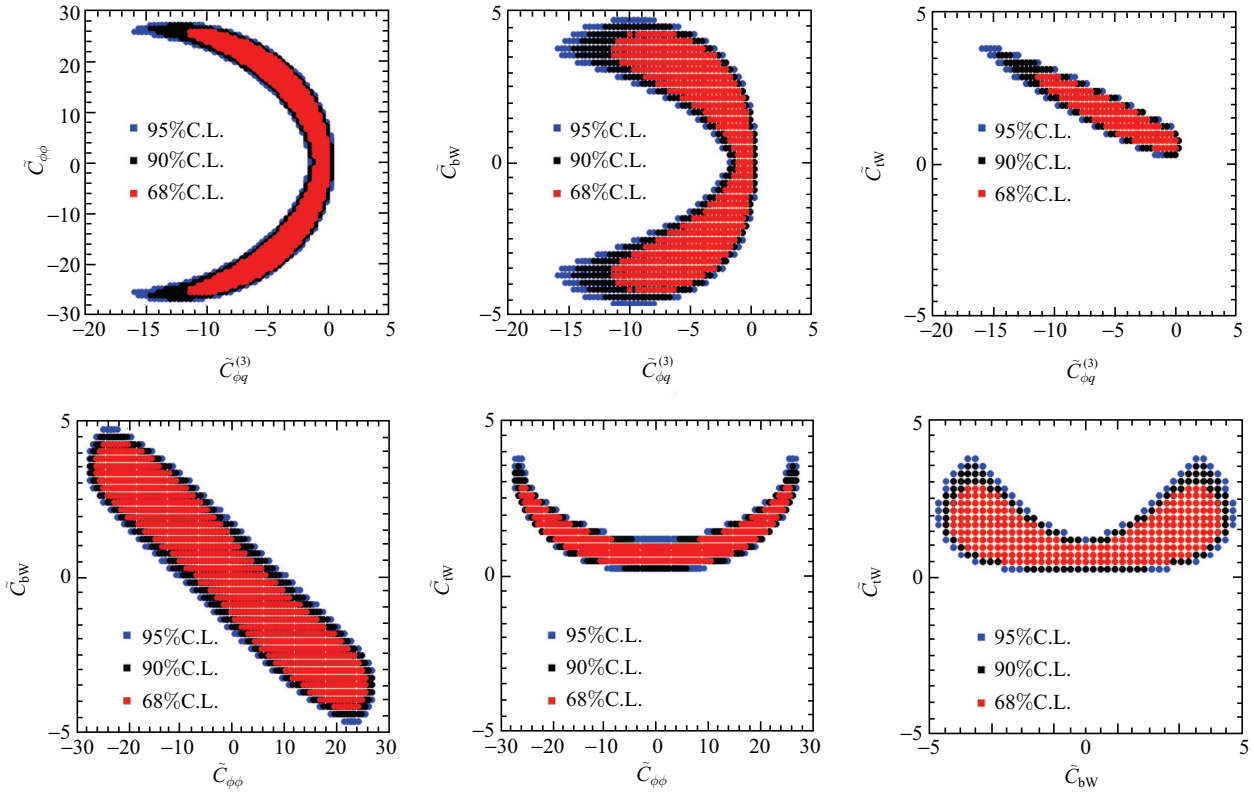

Fig. 3. (color online) Allowed parameter space at 68%, 90% and 95% confidence levels for parameter $\widetilde{C}_i$, where $\widetilde{C}_i \equiv C_i(1\ {\rm TeV}/\Lambda)^2$.

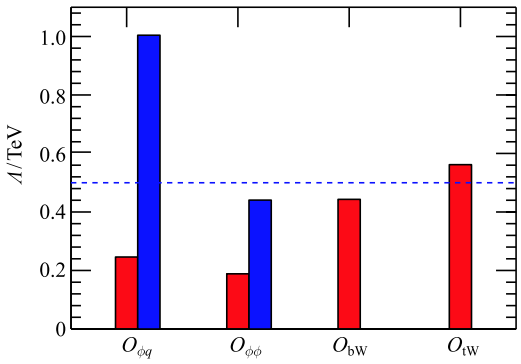

Fig. 4. (color online) Limits on the cut-off scale Λ_i of each individual operator O_i with the Wilson coefficient $|C_i| = 1$. The red bars represent those limits when all four operators contribute simultaneously, while the blue bars display those limits obtained when we consider one parameter at a time. The cut-off scale $\Lambda = 500$ GeV is also plotted for reference; see the horizontal blue-dashed line.

3.3 Constraints on the effective Wtb couplings and operators in 2-dimensional subspaces

So far we have considered the full correlations among the four effective couplings and explored the allowed parameter space of the effective Wtb couplings. However, not all but only some of the effective couplings are nonzero in many NP models.

In those cases, we limit the parameter space to subspaces and redo the global analysis in those subspaces. Based on the NP models to be discussed, we perform the following parameter scans:

1) We scan the 1-dim parameter space by considering either f_1^L or f_1^R only. For example, in the $G(221)$ models and vector-like quark models, the dominant correction is in the coupling f_1^L or f_1^R, depending on the detail of the models (see Tables 4 and 6).

2) We also consider the case where both f_1^L and f_1^R are modified, e.g., the vector-like quark doublet (T, B) model and triplet cases, shown in Table 6.

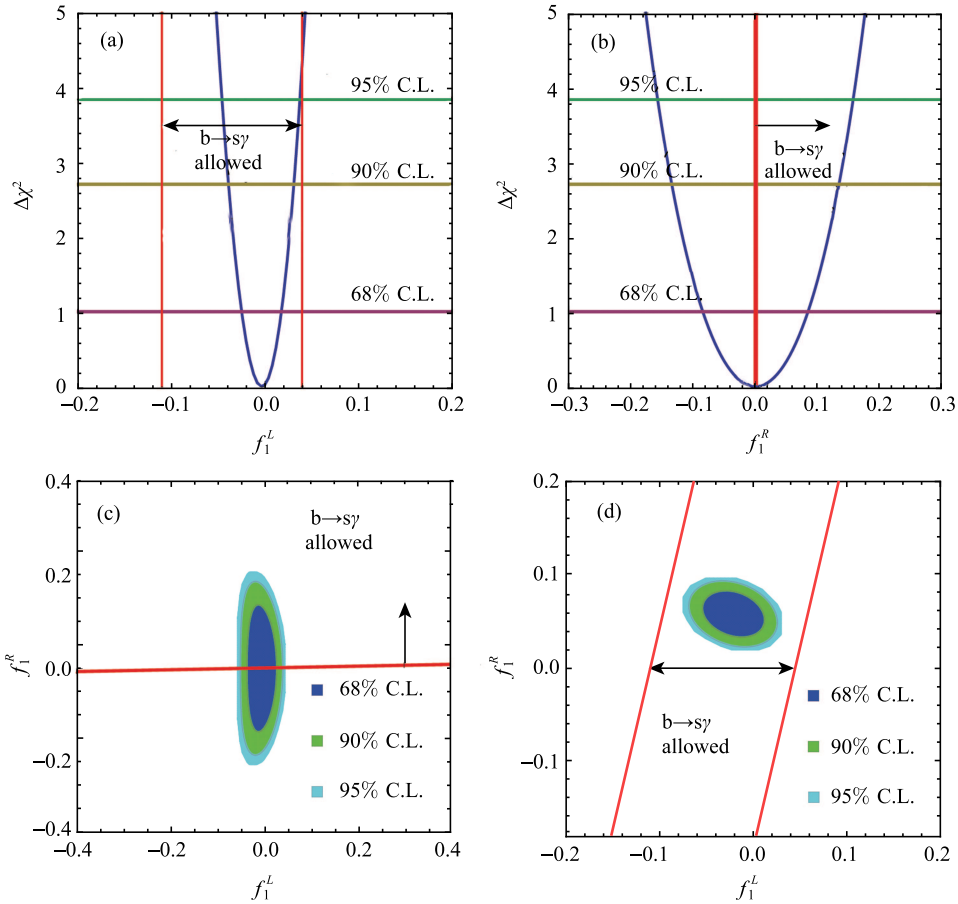

Fig. 5. (color online) Allowed parameter space at 68%, 90% and 95% confidence levels for the effective couplings in the subspace. (a) and (b) correspond to the 1-dim parameter space f_1^L and f_1^R, respectively. The contour plots (c) and (d) correspond to the cases where only f_1^L, f_1^R and f_1^L, f_2^R are modified, respectively. The red lines denote the constraints from $b \to s\gamma$; detailed analyses of those constraints have been given in Ref. [84].

3) Another case is where both f_1^L and f_2^R are modified. A typical example is MSSM. Ref. [85] has shown that the anomalous Wtb couplings have the following features $f_1^L > f_2^R \gg f_1^R, f_2^L$ in the MSSM.

The results of the parameter scan are plotted in Fig. 5. In our analysis, we include the constraints from $b \to s\gamma$ [84] and update the limits of those anomalous couplings using the updated experimental data [86], see Table 3. From Table 3, we note that $b \to s\gamma$ imposes strong constraints on f_1^R and f_2^L, which can be viewed as the results of m_b suppression for the right-handed bottom quark in the pure left-handed Wtb vertex, while the amplitude is enhanced by m_t if the right-handed Wtb vertex exists [33, 84, 87–90]. We also note that the central value of f_1^L is negative, while f_1^R is zero in that case (see Fig. 5(a) and Fig. 5(b)). This is because the cross section is proportional to $(1+f_1^L)^2$, and the minimal χ^2 is dominant, determined by the most precise experiment. In this case, the most precise experiment is the measurement of the t channel cross section (see Table 2). However, the central value of the experiment is smaller than the approximate NNLO SM prediction (see Table 1). Therefore the best-fitted value of f_1^L is negative. For the f_1^R case, the cross section is proportional to $(1+(f_1^R)^2)$, thus the minimal χ^2 corresponds to the SM case, and the central value of f_1^R is zero. As shown in Fig. 5(a) and Fig. 5(b), f_1^L and f_1^R are constrained to be $-0.05 < f_1^L < 0.025$ and $|f_1^R| < 0.13$ at 90% C.L. by direct experimental measurements of the top quark. Similarly, we translate the allowed region of the effective couplings to the coefficients $\widetilde{C}_i$ of dimension-6 operators, with the results shown in Fig. 6.

Table 3. The current 95% C.L. bound on the structure of the Wtb vertices from $\bar{B} \to X_s\gamma$ with $\mu_0 = 160$ GeV, where μ_0 is the top quark and electroweak gauge boson decoupling scale [84]. The branching ratio $\mathcal{B}(\bar{B} \to X_s\gamma)_{E_\gamma > 1.6\ \mathrm{GeV}} = (3.43 \pm 0.21 \pm 0.07) \times 10^{-4}$ is used [86].

bound	f_1^L	f_1^R	f_2^L	f_2^R
upper	0.04	0.0021	0.0011	0.19
lower	−0.11	−0.0008	−0.0004	−0.48

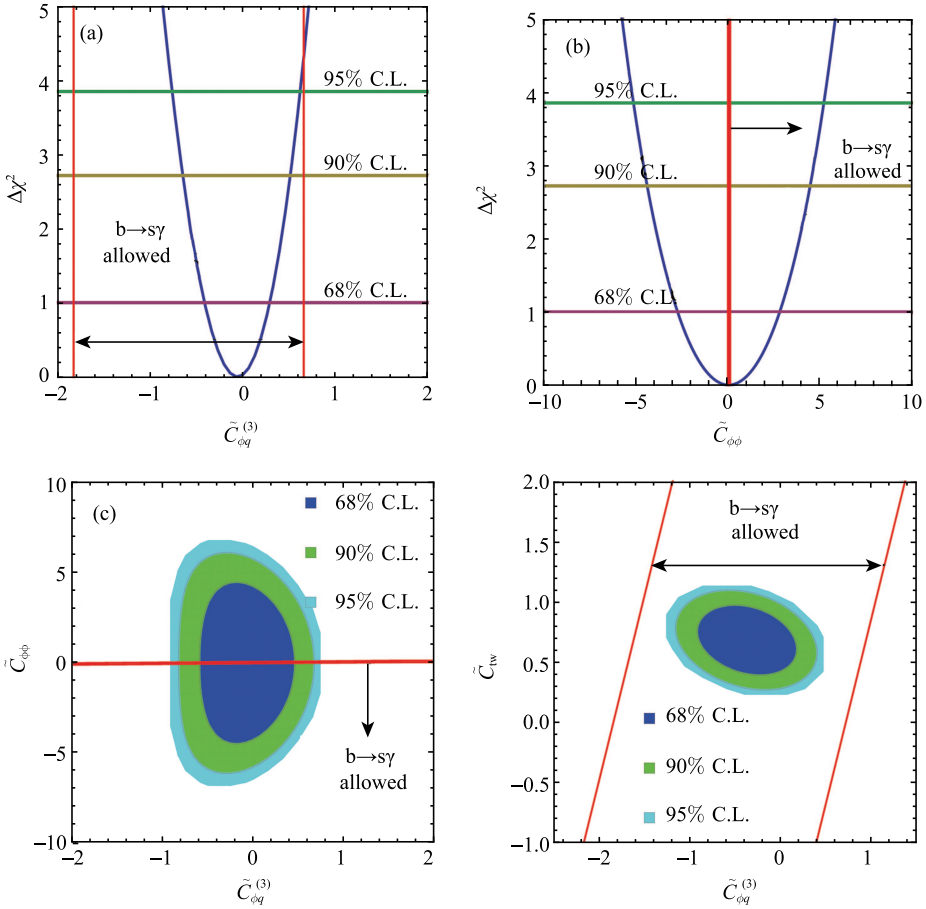

Fig. 6. (color online) Allowed parameter space at 68%, 90% and 95% confidence levels for the parameter $\widetilde{C}_i$ in the subspace. (a) and (b) correspond to the 1-dim parameter space $\widetilde{C}_{\phi q}^{(3)}$ and $\widetilde{C}_{\phi\phi}$, respectively. The contour plots (c) and (d) correspond to the cases where $\widetilde{C}_{\phi q}^{(3)}$, $\widetilde{C}_{\phi\phi}$ and $\widetilde{C}_{\phi q}^{(3)}$, $\widetilde{C}_{tW}$ are both modified, respectively. The red lines denote the constraints from $b \to s\gamma$.

4 Top couplings in new physics models

As mentioned in Section 1, the Wtb coupling can be modified by many kinds of NP models. In this section, we discuss the constraints from the effective Wtb couplings in several NP models.

4.1 $G(221)$ models

The $G(221)$ models [5, 91–102] represent a class of NP models with $SU(2)_1\otimes SU(2)_2\otimes U(1)_X$ gauge symmetry. There are two breaking patterns: $SU(2)_L\otimes SU(2)_2\otimes U(1)_X \to SU(2)_L\otimes U(1)_Y$ (BP-I) or $SU(2)_1\otimes SU(2)_2\otimes U(1)_Y \to SU(2)_L\otimes U(1)_Y$ (BP-II). In BP-I, a scalar doublet field $\Phi\sim(1,2)_{1/2}$ or a triplet field $\Sigma\sim(1,3)_1$ with a vacuum expectation value (VEV) u is introduced to induce the symmetry breaking of $SU(2)_L\otimes SU(2)_2\otimes U(1)_X \to SU(2)_L\otimes U(1)_Y$ at the TeV scale, where the numbers in the parentheses are the quantum numbers of $SU(2)_1$ and $SU(2)_2$, respectively, and the numbers in the subscripts of the parentheses are the $U(1)_X$ charges. At the electroweak scale, the symmetry is further broken by a bi-doublet scalar field $H\sim(2,\bar{2})_0$ with two VEVs v_1 and v_2. We introduce $v=\sqrt{v_1^2+v_2^2}$ and a mixing angle $\tan\beta=v_1/v_2$ for convenience. In BP-II, the breaking of $SU(2)_1\otimes SU(2)_2\to SU(2)_L$ is induced by a scalar bi-doublet $\Phi\sim(2,\bar{2})_0$ with one VEV u at TeV scale, and the electroweak symmetry breaking is induced by a Higgs doublet $H\sim(2,1)_{1/2}$ with VEV v. After symmetry breaking, the new gauge boson W′ obtains mass and mixes with the SM gauge boson W. For simplicity, we define a new mixing angle ϕ,

$$\tan\phi=\frac{g_x}{g_2}, \qquad (\mathrm{BP-I}) \tag{24}$$

$$\tan\phi=\frac{g_1}{g_2}, \qquad (\mathrm{BP-II}) \tag{25}$$

where g_1, g_2 and g_x are the gauge couplings of $SU(2)_1$, $SU(2)_2$ and $U(1)_X$, respectively. The gauge bosons' masses are

$$M^2_{\mathrm{W}^\pm}=\frac{e^2v^2}{4s^2_{\mathrm{W}}}\left(1-\frac{s^2_{2\beta}}{x}\right), \qquad M^2_{\mathrm{W}'^\pm}=\frac{e^2v^2}{4c^2_{\mathrm{W}}s^2_\phi}\left(x+1+\frac{s^2_\phi s^2_{2\beta}c^2_{\mathrm{W}}}{xs^2_{\mathrm{W}}}\right), \qquad (\mathrm{BP-I}) \tag{26}$$

$$M^2_{\mathrm{W}^\pm}=\frac{e^2v^2}{4s^2_{\mathrm{W}}}\left(1-\frac{s^4_\phi}{x}\right), \qquad M^2_{\mathrm{W}'^\pm}=\frac{e^2v^2}{4s^2_{\mathrm{W}}s^2_\phi c^2_\phi}\left(x+s^4_\phi+\frac{s^6_\phi c^2_\phi}{x}\right), \qquad (\mathrm{BP-II}) \tag{27}$$

where e denotes the electron charge and $x=u^2/v^2$. We also abbreviate the trigonometric functions as $c_\phi\equiv\cos\phi$, $s_\phi\equiv\sin\phi$, $s_{2\beta}\equiv\sin2\beta$, $c_{\mathrm{W}}\equiv\cos\theta_w$ and $s_{\mathrm{W}}\equiv\sin\theta_{\mathrm{W}}$ where θ_{W} is the SM weak mixing angle.

The third generation quarks play a special role in several $G(221)$ models, and the Wtb couplings are modified through the mixing effects between the new gauge boson W′ and SM gauge boson W at tree-level. In this work, we will use the left-right model [91–93], un-unified model [94, 95] and top-flavor model [96–98, 103] as examples to discuss the impact of the Wtb measurements on those NP models. The charge assignments of the third generation quark fields under the $G(221)$ gauge groups and the detailed expressions of f_1^L and f_1^R of those NP models are listed in Table 4.

Table 4. The charge assignments of the third generation quark fields under the $G(221)$ gauge groups and the gauge couplings of the third generation quarks with W boson in several $G(221)$ models.

model	$SU(2)_1$	$SU(2)_2$	$U(1)_X$	f_1^L	f_1^R
left-right	$\begin{pmatrix}t_L\\b_L\end{pmatrix}$	$\begin{pmatrix}t_R\\b_R\end{pmatrix}$	$\frac{1}{6}$	0	$\frac{\sin2\beta}{x}$
un-unified	$\begin{pmatrix}t_L\\b_L\end{pmatrix}$	–	$\frac{1}{6}$	$---\frac{s^4_\phi}{x}$	0
top-flavor	—	$\begin{pmatrix}t_L\\b_L\end{pmatrix}$	$\frac{1}{6}$	$\frac{s^2_\phi c^2_\phi}{x}$	0

We discuss the impact of the effective Wtb coupling measurements on the parameter space of the $G(221)$ models. Figure 7 presents the allowed parameter space at 68%, 90% and 95% C.L., respectively in the left-right model in BP-I and the un-unified and top-flavor models in BP-II. In the left-right model, we show the allowed parameter space in the $(M_{\mathrm{W}'},s_\beta)$ plane for $s_\phi=0.1$ and $s_\phi=0.9$ in Fig. 7(a) and Fig. 7(b), respectively. Figure 7(a) shows that, for $s_\phi=0.1$, a vast parameter space of moderate s_β and smaller $M_{\mathrm{W}'}$ is not allowed by the highly constrained right-handed Wtb coupling, see Table 4. For a larger $s_\phi=0.9$, the constraint for $M_{\mathrm{W}'}$ tends to be looser, see Fig. 7(b). The reason is that the gauge coupling of the SM $U(1)_Y$ is related to the gauge couplings g_2 and g_x as $1/g_Y^2=1/g_2^2+1/g_X^2$. Thus, g_Y is approximately equal to g_X in the limit $s_\phi\to0$, which corresponds to the decoupling region. The shape of the allowed parameter space for $s_\phi=0.9$ is the same as that of $s_\phi=0.1$ in the small $M_{\mathrm{W}'}$ region.

Figures 7(c–e) display the allowed parameter space in the plane of $(M_{\mathrm{W}'},s_\phi)$ for $s_\beta=0.1,0.5,0.9$, which shows that $M_{\mathrm{W}'}$ is not sensitive to s_β. This is because s_β only induces mixing between the gauge boson W and W′ (see Eq. (26)), and the primary source of the mass of the W′ is from the first step breaking, which is proportional to the VEV u [5].

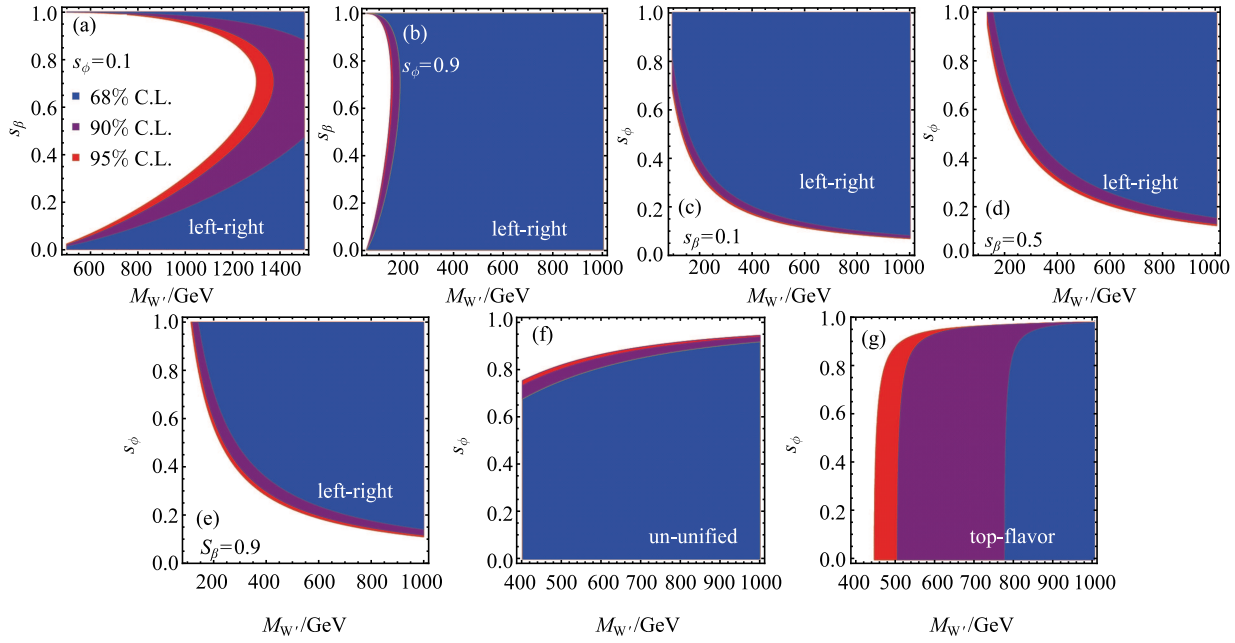

Fig. 7. (color online) Allowed parameter space at 68%, 90% and 95% confidence levels for several G(221) models in the $(M_{W'}, s_\beta)$ or $(M_{W'}, s_\phi)$ plane. Sub-figures (a-e) correspond to the left-right model with $s_\phi = 0.1,\ 0.9$ (a, b) or $s_\beta = 0.1,\ 0.5,\ 0.9$ (c, d, e). The contour plots (f) and (g) correspond to un-unified and top-flavor models, respectively.

In the un-unified and top-flavor models, only the left-handed Wtb coupling is modified. The allowed parameter space in the $(M_{W'}, s_\phi)$ plane is shown in Fig. 7(f) (un-unified model) and Fig. 7(g) (top-flavor model). We note that the shape in the large s_ϕ region is different between the un-unified model and top-flavor model. The difference can be understood from the effective Wtb couplings shown in Table 4. The effect consists of two factors: one is W′tb coupling, the other is W-W′ mixing. The former is different in the two models, but the latter is the same. The gauge coupling of the heavy gauge boson W′ with the top and bottom quarks is proportional to $\tan\phi$ in the un-unified model, while it is proportional to $\cot\phi$ in the top-flavor model. Thus, larger s_ϕ is allowed in the top flavor model compared with the un-unified model. Another important feature in the top-flavor model is that the constraint on $M_{W'}$ is not sensitive to the parameter s_ϕ, as shown in Fig. 7(g). In the model, f_1^L is modified by the W′ mass, which is proportional to $x/(s_\phi^2 c_\phi^2)$.

In order to validate our EFT prescription of the NP effects, W′ should be heavy. Figure 7 shows the constraints of $G(221)$ models from Wtb measurements are weak when new gauge bosons are heavier than 800 GeV. The constraints from low energy precision measurements and direct searches at the Tevatron and LHC have pushed the new heavy gauge bosons to several TeV [6]. Therefore, it is difficult to further constrain the parameter space by the Wtb measurements.

4.2 Vector-like quark models: T and B

The vector-like quark (VLQ) is a common ingredient of many NP models. In order to keep the discussion general, we employ an effective Lagrangian approach to parametrize the effects of vector-like quarks. The quantum numbers of the new VLQ with respect to the $SU(2)_L \otimes U(1)_Y$ gauge group are summarized in Table 5 [7–10].

Table 5. The quantum numbers of the vector-like quarks under the SM $SU(2)_L \otimes U(1)_Y$ gauge symmetry. The electric charge of the quark is obtained by $Q = T_3 + Y$, where T_3 is the third component of the isospin, and Y is the hypercharge of $U(1)_Y$.

model	T	B	$\begin{pmatrix} X \\ T \end{pmatrix}$	$\begin{pmatrix} T \\ B \end{pmatrix}$	$\begin{pmatrix} B \\ Y \end{pmatrix}$	$\begin{pmatrix} X \\ T \\ B \end{pmatrix}$	$\begin{pmatrix} T \\ B \\ Y \end{pmatrix}$
$SU(2)_L$	1	1	2	2	2	3	3
$U(1)_Y$	$\frac{2}{3}$	$-\frac{1}{3}$	$\frac{7}{6}$	$\frac{1}{6}$	$-\frac{5}{6}$	$\frac{2}{3}$	$-\frac{1}{3}$

The Wtb coupling is modified by the mixing between the top quark or bottom quark with their corresponding vector-quark partner, e.g. the top partner T or bottom partner B. After spontaneous symmetry breaking, the mass terms of the top quark and top partner T in the

singlet or triplet models are [9]

$$\mathcal{L}^t_{\rm mass} = -\frac{y_t v}{\sqrt{2}}\bar{t}_L t_R - x_t \bar{t}_L T_R - M\bar{T}_L T_R + {\rm h.c.}, \quad (28)$$

where y_t is the Yukawa coupling of top quark in the SM, x_t represents the mixing parameter between t and T, and M denotes the VLQ's mass.

In the case of doublet VLQ models, the mass terms are [9]

$$\mathcal{L}^t_{\rm mass} = -\frac{y_t v}{\sqrt{2}}\bar{t}_L t_R - x_t \bar{T}_L t_R - M\bar{T}_L T_R + {\rm h.c.}. \quad (29)$$

The weak and mass eigenstates can be related by 2×2 unitary matrices,

$$\begin{pmatrix} t_{L,R} \\ T_{L,R} \end{pmatrix} = \begin{pmatrix} c^t_{L,R} & s^t_{L,R} \\ -s^t_{L,R} & c^t_{L,R} \end{pmatrix} \begin{pmatrix} t'_{L,R} \\ T'_{L,R} \end{pmatrix}, \quad (30)$$

where $c^t_{L,R}$ and $s^t_{L,R}$ denote the cosine and sine of the mixing angles between left-handed and right-handed top quark ${\rm t}_{L,R}$ with the top partner ${\rm T}_{L,R}$. In this section, we use the prime in the superscript on mass eigenstates to distinguish from the weak eigenstates. After diagonalizing the mass matrices, we can rewrite the mixing angles according to the parameters in Eqs. (28) and (29).

In the case of singlet and triplet VLQ models

$$s^t_L = \frac{Mx_t}{\sqrt{(M^2-m_{\rm t}^2)^2+M^2x_t^2}}, \quad s^t_R = \frac{m_{\rm t}}{M}s^t_L. \quad (31)$$

For the doublet VLQ models

$$s^t_R = \frac{Mx_t}{\sqrt{(M^2-m_{\rm t}^2)^2+M^2x_t^2}}, \quad s^t_L = \frac{m_{\rm t}}{M}s^t_R, \quad (32)$$

where m_t is the top quark mass. The mass of the heavy top partner is

$$M^2_{\rm T} = M^2\left(1+\frac{x_t^2}{M^2-m_{\rm t}^2}\right). \quad (33)$$

We can obtain similar formulae in the bottom quark sector, and use $m_{\rm b}$ and $x_{\rm b}$ to denote the bottom quark mass and mixing parameter between bottom quark and bottom partner B hereafter. In the triplet VLQ models, $s^t_{L/R}$ is correlated with $s^b_{L/R}$ as the mixing parameters x_t and x_b are linearly related to each other. For example, in the (X,T,B) model [9],

$$\mathcal{L}_{(X,T,B)} = -\frac{y_t v}{\sqrt{2}}\bar{t}_L t_R - x_t\bar{t}_L T_R - x_b\bar{b}_L B_R - M(\bar{T}_L T_R + \bar{B}_L B_R + \bar{X}_L X_R) + {\rm h.c.}, \quad (34)$$

with $x_{\rm b} = \sqrt{2}x_t$, and in the (T,B,Y) model [9],

$$\mathcal{L}_{(T,B,Y)} = -\frac{y_t v}{\sqrt{2}}\bar{t}_L t_R - x_t\bar{t}_L T_R + x_{\rm b}\bar{b}_L B_R - M(\bar{T}_L T_R + \bar{B}_L B_R + \bar{Y}_L Y_R) + {\rm h.c.}, \quad (35)$$

with $x_{\rm t} = \sqrt{2}x_{\rm b}$. After diagonalizing the mass matrices, we obtain the couplings of the gauge boson fields to the third generation quarks,

$$\mathcal{L}_{\rm Zbb} = \frac{g}{2c_{\rm W}}\bar{b}'\gamma^\mu\left(-f^L_b P_L - f^R_b P_R + \frac{2}{3}s^2_W\right)b' Z_\mu. \quad (36)$$

The couplings $f_1^{L,R}$ and $f_b^{L,R}$ for all 7 models are listed in Table 6, see also Ref. [10].

Table 6. The Wtb and Zbb couplings in 7 models, where $c^t_L(s^t_L)$ and $c^b_L(s^b_L)$ denote the cosine (sine) of the mixing angles of left-handed top quark and bottom quark with their heavy partners, respectively. Similarly, s^t_R and s^b_R are the sine of the mixing angles of right-handed top quark and bottom quark with their heavy partners, respectively.

model	(T)	(B)	(X,T)	(T,B)	(B,Y)	(X,T,B)	(T,B,Y)
f_1^L	c^t_L-1	c^b_L-1	c^t_L-1	$c^t_Lc^b_L+s^t_Ls^b_L-1$	c^b_L-1	$c^t_Lc^b_L+\sqrt{2}s^t_Ls^b_L-1$	$c^t_Lc^b_L+\sqrt{2}s^t_Ls^b_L-1$
f_1^R	0	0	0	$s^t_Rs^b_R$	0	$\sqrt{2}s^t_Rs^b_R$	$\sqrt{2}s^t_Rs^b_R$
f_b^L	1	$(c^b_L)^2$	1	1	$(c^b_L)^2-(s^b_L)^2$	$1+(s^b_L)^2$	$(c^b_L)^2$
f_b^R	0	0	0	$(s^b_R)^2$	-$(s^b_L)^2$	$2(s^b_R)^2$	0

4.2.1 Mixing angles

Using the results of Section 3, we translate the allowed region of the effective Wtb couplings to the parameter space of VLQ models at 68%, 90% and 95% C.L., respectively; see Fig. 8. In the triplet and singlet models, VLQs mainly couple to the left-handed top or bottom quark, while in the doublet models they couple to the right-handed top or bottom quark. As a result, $s^{t/b}_L \gg s^{t/b}_R$ in the triplet model, and $s^{t/b}_R \gg s^{t/b}_L$ in the doublet model. It is, therefore, convenient to neglect the smaller mixing angles in our parameter scan. Figure 8(a) shows the allowed parameter space of (s^t_R, s^b_R) in the doublet (T,B) model. It yields the hyperbola contour region on the plane, which is determined by the right-handed Wtb coupling $f_1^R = s^t_Rs^b_R$. Figure 8(b) displays the contour on the plane of (s^t_L, s^b_L) in the triplet models, and the allowed parameter space is symmetric about $s^t_L \leftrightarrow s^b_L$ and $s^t_L \leftrightarrow -s^b_L$. Such behavior can be understood from

the deviation of the left-handed Wtb coupling between the triplet models and the SM

$$f_1^L = \sqrt{1-(s_L^t)^2}\sqrt{1-(s_L^b)^2} + \sqrt{2}s_L^t s_L^b - 1. \quad (37)$$

Furthermore, the upper limit of f_1^L determines the shape of the parameter contour in the top-right and bottom-left regions, and the lower limit of f_1^L determines the boundary of the parameter space in the top-left and bottom-right regions. Note that only one mixing angle exists in the singlet models T and B, and in the doublet models (X,T) and (B,Y). Figure 8(c) shows the allowed parameter space of the sole mixing angle, s_L^t or s_L^b, which indicates $|s_L^{t,b}| < 0.34$ at 95% C.L..

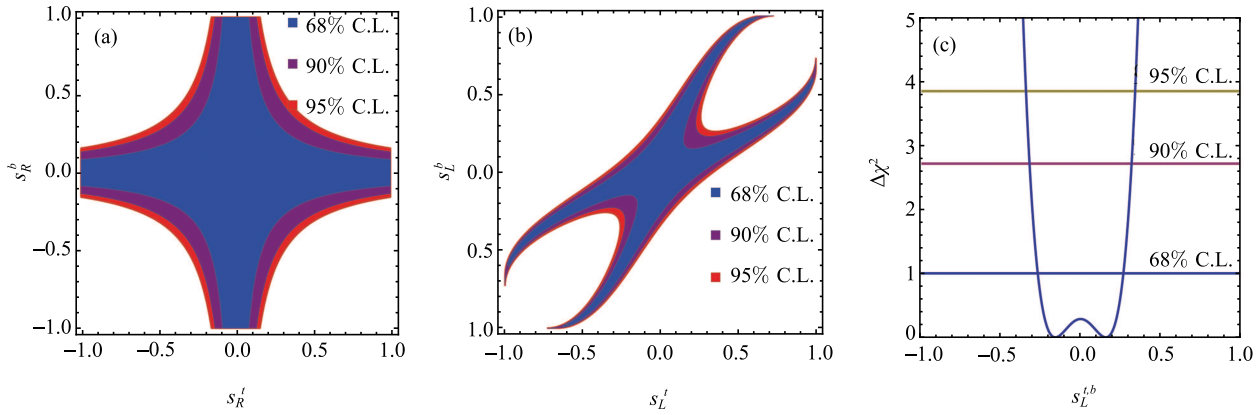

Fig. 8. (color online) Allowed parameter space at 68%, 90% and 95% confidence levels for the VLQ models: (a) doublet (T,B) model; (b) triplet models; (c) singlet, doublet (X,T), (B,Y) models.

4.2.2 Mixing angles versus $M_{\rm T,B}$

We note that the constraints from the Wtb measurements on the parameter space of the VLQ models are weak. However, the left-handed top quark and bottom quark form a $SU(2)_L$ weak doublet, and the left-handed $\mathrm{Wt}_L\mathrm{b}_L$ coupling is always related to the left-handed $\mathrm{Zt}_L\mathrm{t}_L$ and $\mathrm{Zb}_L\mathrm{b}_\mathrm{L}$ couplings. The R_b and A_{FB}^b measurements at LEP-II [104] impose severe constraints on the $\mathrm{Zb}_L\mathrm{b}_\mathrm{L}$ couplings, which yields a correlation between $\mathrm{Zt}_L\mathrm{t}_L$ and $\mathrm{Wt}_L\mathrm{b}_L$ [40, 105]. To fully constrain the allowed parameter space of the VLQ models, it is necessary to include the Zbb and Ztt couplings in the analysis. The complete study will be presented elsewhere. In this work, we will allow a variation of -0.2% and $+1\%$ for the left-handed $\mathrm{Zb}_L\mathrm{b}_L$ coupling, while in the right-handed case, -5% and $+20\%$ is used [9].

Another important constraint comes from the Peskin-Takeuchi parameters $\hat{S}$, $\hat{T}$ and $\hat{U}$ [106]. The contribution of an arbitrary number of vector-like singlet and doublet quarks to the $\hat{S}$, $\hat{T}$ and $\hat{U}$ parameters have been calculated in Ref. [107], and is generalised to arbitrary couplings in Ref. [108]. In our work, we calculate the $\hat{T}$ parameter of all possible VLQ models. Our analytical results are consistent with Ref. [109]. The definition of the $\hat{T}$ parameter is

$$\alpha\hat{T} = \frac{\Pi_{\rm WW}(0)}{m_{\rm W}^2} - \frac{\Pi_{\rm ZZ}(0)}{m_{\rm Z}^2}, \quad (38)$$

where the notation $\Pi_{\rm WW}(0)$ and $\Pi_{\rm ZZ}(0)$ denotes the vacuum polarization amplitudes of the W loop and Z loop at zero momentum, respectively, α is the fine-structure constant and $m_{\rm W/Z}$ is the mass of the W or Z boson. In the NP model, the contribution of the $\hat{U}$-parameter is usually very small and can be neglected. Fixing $\hat{U}=0$, the $\hat{T}$ parameter is obtained [110]

$$\Delta\hat{T} = \hat{T} - \hat{T}_{\rm SM} = 0.10 \pm 0.07, \quad (39)$$

where the reference top quark and Higgs boson masses are $m_{\rm t} = 173$ GeV and $m_{\rm H} = 125$ GeV.

We present the allowed regions of the VLQ models in Figs. 9–12. In order to better understand the impact of various bounds, we separate the constraints into different categories: the Wtb coupling constraint at 95% C.L. (green region), $\hat{T}$ parameter constraint at 95% C.L. (red region) and Zbb coupling constraint (black line). The top and bottom quark partners must be heavy in order to validate our EFT prescription of the NP effects. Currently, both the ATLAS and CMS collaborations have searched for various VLQs and imposed bounds on the heavy quark's mass [111, 112]. The current mass limit of top partners are $m_{\rm T} > 660$ GeV for singlet (T) and triplet (X,T,B), $m_{\rm T} > 855$ GeV for doublet (X,T) and doublet (T,B), and $m_{\rm T} > 878$ GeV for triplet (T,B,Y). Bounds on the bottom quark partner's mass are $m_{\rm B} > 735$ GeV for singlet (B), $m_{\rm B} > 450$ GeV for doublets (T,B), (B,Y) and triplet (T,B,Y), and $m_B > 408$ GeV for triplet (X,T,B) (see the purple lines).

We plot in Figs. 9–12 the effects of the Wtb mea-

surements on the parameter space of the VLQ models. We note the following common features when comparing different experimental constraints. There is no direct constraint on the heavy VLQ's mass from the Wtb measurements, as f_1^L and f_1^R depend only on the quark mixing angles (see Table 6). For most of the parameter space of the VLQ models, the bounds from the Wtb coupling measurements are weak. We also consider the measurements of the Zbb coupling if a bottom-quark partner is present. The Zbb coupling was measured very precisely at LEP II [104], such that it leads to a much tighter bound than the Wtb coupling measurements at the Tevatron and LHC.

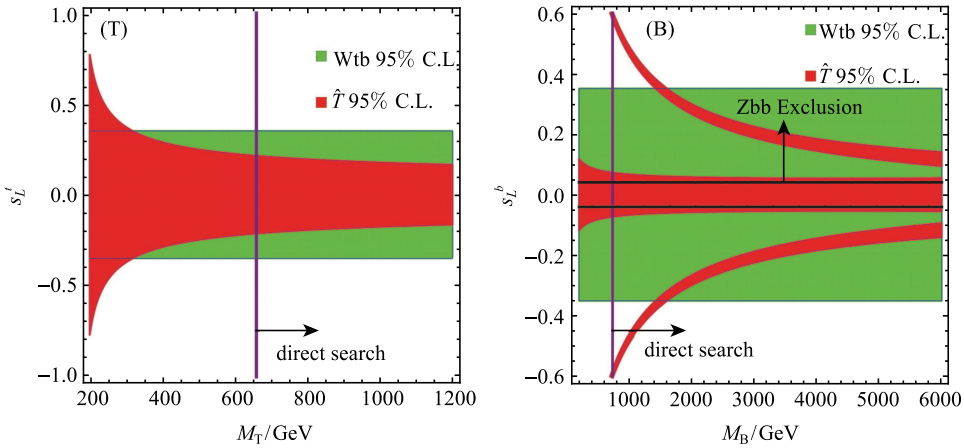

Fig. 9. (color online) Allowed parameter space at 95% C.L. of the singlet T model in the plane of (M_T, s_L^t) and of the singlet B model in the plane of (M_B, s_L^b) after including indirect and direct constraints: Wtb coupling (green region), $\hat{T}$ parameter (red region), Zbb coupling (black line), direct search at the LHC (purple line).

Figure 9 shows the allowed region of the singlet T quark model (left) and the singlet B quark model (right). In the singlet T model, the light T quark contributes largely to the $\hat{T}$ parameter, thus a large quark mixing angle is needed to respect the $\hat{T}$ parameter constraints [113], and the bound from the Wtb measurements plays an important role for a light T quark, say $M_T \sim 300$ GeV,

$$\frac{\Delta\hat{T}_T}{\hat{T}^F_{\rm SM}} = (s_t^L)^2\left[-\left(1+(c_t^L)^2\right) +(s_t^L)^2\frac{M_T^2}{m_t^2}+(c_t^L)^2\frac{2M_T^2}{M_T^2-m_t^2}\ln\frac{M_T^2}{m_t^2}\right], \quad (40)$$

where $\hat{T}^F_{\rm SM} \equiv 3/(16\pi s_W^2 c_W^2)(m_t^2/m_Z^2)$ denotes the contributions from the third generation SM quarks. For a heavy T quark, the $\hat{T}$ parameter constraint dominates over the Wtb coupling, Fig. 9 also shows the allowed parameter space of the singlet B model. We note that, different from the singlet T model, a two-fold contour of the $\hat{T}$ parameter occurs. The reason is that $\Delta\hat{T}_T > 0$ in the singlet T model, and there is no constraint from the lower limit of the $\hat{T}$ parameter. That result is obvious in the heavy mass region $M_T \gg m_t$. In the small mass region ($M_T \sim m_t$), Eq. (40) can be written as

$$\frac{\Delta\hat{T}_T}{\hat{T}^F_{\rm SM}} = (s_t^L)^2\left(\frac{M_T^2}{m_t^2}-1\right)\left(1+(c_t^L)^2\right), \quad (41)$$

which shows the $\Delta\hat{T}_T$ is positive if $M_T > m_t$. But the $\Delta\hat{T}$ is not always positive in the singlet B, thus both the upper and lower limits of the $\hat{T}$ parameter give a constraint on the parameter space of the singlet B [107],

$$\frac{\Delta\hat{T}_B}{\hat{T}^F_{\rm SM}} = (s_b^L)^2\left[(s_b^L)^2\frac{M_B^2}{m_t^2}-\frac{2M_B^2}{M_B^2-m_t^2}\ln\frac{M_B^2}{m_t^2}\right]. \quad (42)$$

We also note that the two-fold contours of the $\hat{T}$ parameter in the singlet B model tend to overlap each other when $M_B > 5.5$ TeV due to the decoupling of the heavy VLQ.

Figure 10 shows the allowed parameter space of the doublet (X,T) model (left) and the doublet (B,Y) model (right), respectively. The bound on s_L is dominated by the $\hat{T}$ parameter in the heavy VLQ's mass region. It mainly stems from the fact that the top partner or bottom partner of doublet models mainly have right-handed couplings to SM particles, and the left-handed mixing angle is highly suppressed by factor $m_{(t,b)}/M$ in the heavy mass region, see Eq. (32).

The (X,T) quark doublet contributes to the $\hat{T}$ parameter as follows:

$$\frac{\hat{T}_{(X,T)}}{\hat{T}^F_{\rm SM}} = \frac{2}{m_t^2}\left[M_X^2+M_T^2-\frac{2M_X^2M_T^2}{M_X^2-M_T^2}\ln\left(\frac{M_X^2}{M_T^2}\right) +2M_TM_X\left(\frac{M_T^2+M_X^2}{M_T^2-M_X^2}\ln\frac{M_T^2}{M_X^2}-2\right)\right]. \quad (43)$$

The quark mixing yields a mass splitting between the two vector-quarks in the same doublet, which breaks the $SU(2)$ symmetry. Such a breaking effect lead to a non-zero contribution to the $\hat{T}$ parameter.

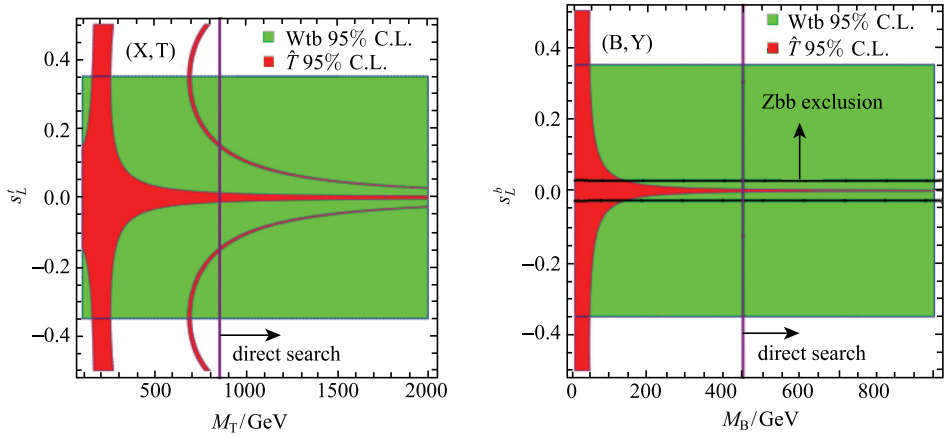

Fig. 10. (color online) Allowed parameter space at 95% C.L. of the (X,T) doublet model in the plane of (M_T, s_L^t) and of the (B,Y) doublet model in the plane of (M_B, s_L^b) after including indirect and direct constraints. The convention is the same as in Fig. 9.

Figure 11 shows the allowed region of a doublet (T,B) model. We note that the Zbb constraint is different between the (s_R^b, M_B) and (s_R^t, M_T) plane. The reason is that the dangerous bound of the Zbb coupling is sensitive to the mixing angle of the bottom quark sector, whereas for the top quark sector, the constraint is indirect and comes from the allowed range of the mass parameter M. However, the mixing parameter x_t is not fixed in the (s_R^t, M_T) plane, therefore the constraint is very weak in the (s_R^t, M_T) plane, see Eq. (32). The constraint from the $\hat{T}$ parameter is sensitive to the parameter x_t, and the constraint is weaker for the smaller x_t. This is because x_t represents the mixing between the top quark and top partner, and the smaller x_t corresponds to the decoupling limit. Note that, even in the case of $s_R^b = 0$, the $\hat{T}$ parameter constraint demands M_B to be larger than several hundred GeV for $x_t = 100$ GeV; see the left-hand figure in Fig. 11. This arises from the non-decoupling effect of the top-quark partner.

The (X,T,B) quark triplet contributes to the $\hat{T}$ parameter as follows:

$$\frac{\hat{T}_{(X,T,B)}}{\hat{T}^F_{\rm SM}} = \frac{4}{m_t^2}\left[M_T^2 + M_B^2 - \frac{2M_T^2 M_B^2}{M_T^2 - M_B^2}\ln\frac{M_T^2}{M_B^2} + 2M_T M_B\left(\frac{M_T^2 + M_B^2}{M_T^2 - M_B^2}\ln\frac{M_T^2}{M_B^2} - 2\right) + M_T^2 + M_X^2 - \frac{2M_T^2 M_X^2}{M_T^2 - M_X^2}\ln\frac{M_T^2}{M_X^2} + 2M_T M_X\left(\frac{M_T^2 + M_X^2}{M_T^2 - M_X^2}\ln\frac{M_T^2}{M_X^2} - 2\right)\right]. \quad (44)$$

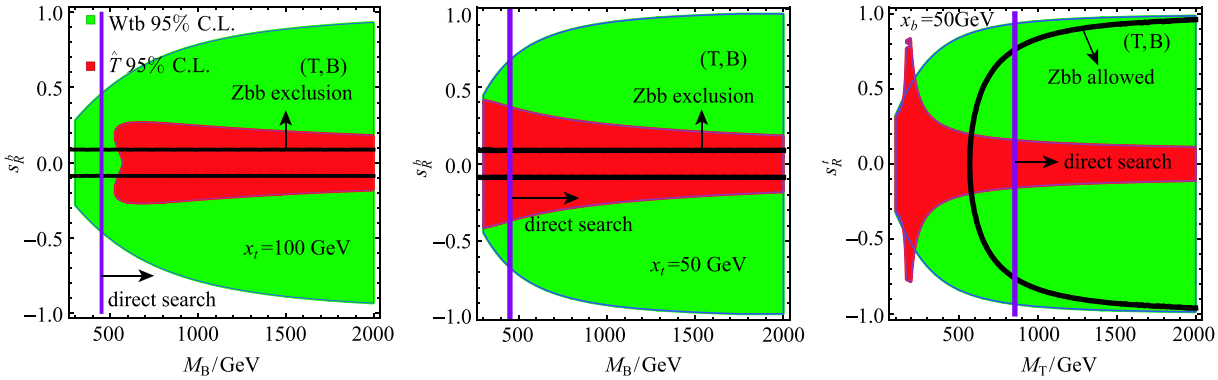

Fig. 11. (color online) Allowed parameter space at 95% C.L. of the SM-like (T,B) doublet model in the plane of (M_B, s_R^b) and (M_T, s_R^t) after including indirect and direct constraints. In the plane (M_B, s_R^b), we fix the top quark sector's mixing parameter $x_t = 100, 50$ GeV, and in the (M_T, s_R^t) plane, the bottom quark sector's mixing parameter x_b is fixed to 50 GeV. The convention is the same as in Fig. 9.

The allowed regions of the triplet (X,T,B) and (T,B,Y) model are shown in Fig. 12. It shows that the allowed parameter space of s_L^t is smaller than that of s_L^b in the heavy mass region. The reason is that the mixing parameter of the bottom quark sector ($\sqrt{2}x_t$) is larger than the top quark sector (x_t), see Eq. (34). A similar result holds for the triplet (T,B,Y) model except that $s_L^b < s_L^t$ in the heavy mass region and the sign of the mixing parameter is opposite ($x_b \to -x_b, x_t \to \sqrt{2}x_b$); see Eq. (35).

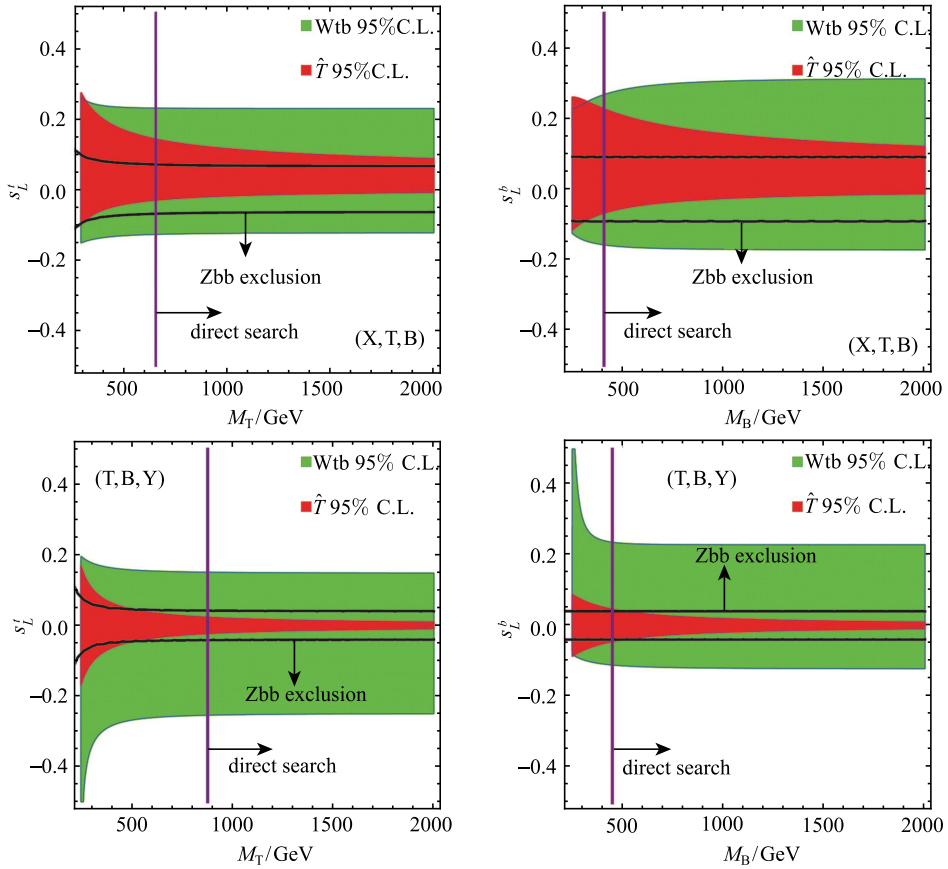

Fig. 12. (color online) Allowed parameter space at 95% C.L. of the (X,T,B) triplet model in the (M_T, s_L^t) plane and of the (T,B,Y) triplet model in the (M_B, s_L^b) plane after including indirect and direct constraints. The convention is the same as in Fig. 9.

4.3 Little Higgs models

Little Higgs models have been proposed to solve the hierarchy problem [114]. The Higgs boson in the Little Higgs models is a pseudo-Goldstone boson arising from the global symmetry breaking at TeV scale and is light due to the collective symmetry breaking mechanism. The one-loop divergence to the Higgs boson mass is cancelled between top-quark and SM gauge bosons and their partners. The Littlest Higgs model was proposed in Ref. [114], based on the $SU(5)/SO(5)$ nonlinear sigma model, with a locally gauged subgroup $G_1 \otimes G_2 = [SU(2)_1 \otimes U(1)_1] \times [SU(2)_2 \otimes U(1)_2]$.

The global symmetry $SU(5)$ is spontaneously broken down to the subgroup $SO(5)$ at the scale of f. At the same time, the gauge symmetry $G_1 \otimes G_2$ is broken down to the diagonal subgroup $SU(2)_L \otimes U(1)_Y$, which is identified as the SM electroweak symmetry.

In the Littlest Higgs model, a vector-like T quark and new heavy gauge boson W′ mix with SM particles and modify the Wtb vertex [12],

$$\mathcal{L}_{\rm Wtb} = \frac{g}{\sqrt{2}}\left[c_L - \frac{v^2}{2f^2}c_\phi^2(c_\phi^2 - s_\phi^2)\right]\bar{t}\gamma^\mu P_L b \mathrm{W}_\mu^+ + \mathrm{h.c.}, \quad (45)$$

where $c_\phi = g_1/\sqrt{g_1^2+g_2^2}$ with g_1 and g_2 are the gauge couplings of the $SU(2)_1$ and $SU(2)_2$, respectively, and c_L is the cosine of the mixing angle of the top quark and T quark.

After considering the Wtb measurements, we plot the allowed parameter space of the Littlest Higgs model in Fig. 13, which shows the allowed parameter space at 68% (blue region), 90% (purple region) and 95% (red region)

C.L., respectively for $f=1$ TeV. It shows that the constraint on the mixing angle s_ϕ is weak but the constraint on s_L is much tighter. This can be understood from Eq. (45), as the contribution of s_ϕ to the Wtb coupling is suppressed by the scale f, while s_L directly modifies the Wtb coupling.

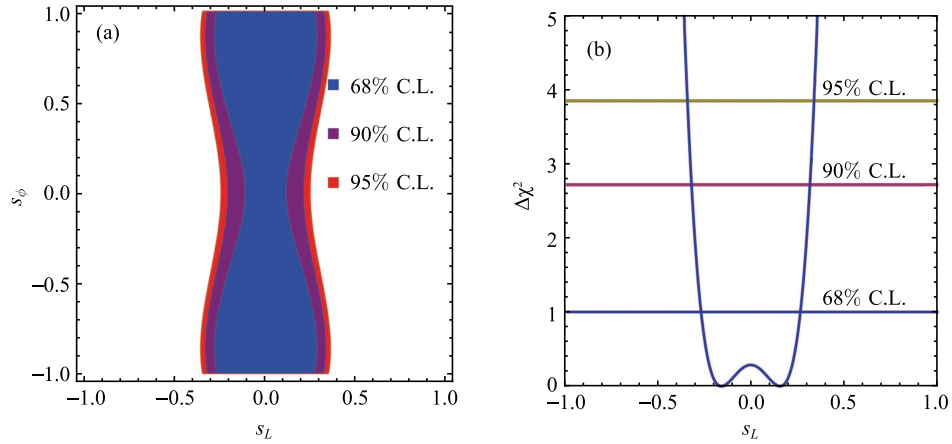

Fig. 13. (color online) Allowed parameter space at 68%, 90% and 95% confidence levels of the Littlest Higgs model (a) and the Littlest Higgs with T parity model (b). s_L is the sine of the mixing angle of the top quark and T quark.

The W′ mixing with the W boson at tree-level modifies the oblique $\hat{T}$ parameter significantly. In order to respect the electroweak precision tests (EWPT), the scale f has to be above several TeV. The current lower bound of f in the Littlest Higgs model at 95% C.L. is 5.1 TeV [115]. Refs. [116–118] introduce a new discrete symmetry to forbid tree-level mixing between W and W′ and relax f down to hundreds of GeV [119]. A simple case is the Littlest Higgs with T-parity (LHT) model, in which the SM particles are even and the new heavy gauge bosons and scalars are odd under T-parity. The only T-parity even non-SM particle is the top partner T and it will contribute to the Wtb coupling through its mixing with the top quark. In the LHT model, the Wtb coupling is [11],

$$\mathcal{L}_{\rm Wtb}=\frac{g}{\sqrt{2}}c_L\bar{t}\gamma^\mu P_L {\rm b}{\rm W}^+_\mu+{\rm h.c.}. \tag{46}$$

Figure 13(b) shows that the effective Wtb coupling measurements require $|s_L|<0.34$ at 95% C.L.

In order to further constrain the mixing angle, we include the Zbb coupling and oblique parameter constraints. To leading order and in the limit $M_{\rm T}\gg m_t\gg m_{\rm W}$, the variation of Zb_Lb_L is given by [120],

$$\delta g^b_L=\frac{g^3}{32\pi^2 c_{\rm W}}\frac{m_{\rm t}^4}{m_{\rm W}^2M_{\rm T}^2}R^2\log\frac{M_{\rm T}^2}{m_t^2}, \tag{47}$$

where $M_{\rm T}$ denotes the T quark mass, and $R=\lambda_1/\lambda_2=s_LM_{\rm T}/m_t$. The correction to the right-handed Zb_Rb_R vertex is negligible in this case. The electroweak precision constraints on the LHT model have been calculated in Ref. [120], which shows that the $\hat{T}$ parameter induced by the T quark loop is much large than the $\hat{S}$ and $\hat{U}$ parameters for the same model parameters. Therefore we will only include the $\hat{T}$ parameter bound in our analysis. The contribution from the heavy T quark is,

$$\frac{\Delta\hat{T}_F}{\hat{T}^F_{\rm SM}}=s_L^2\left[\frac{s_L^2}{x_t}-1-c_L^2-\frac{2c_L^2}{1-x_t}\log x_t\right], \tag{48}$$

where $x_t=m_t^2/M_{\rm T}^2$.

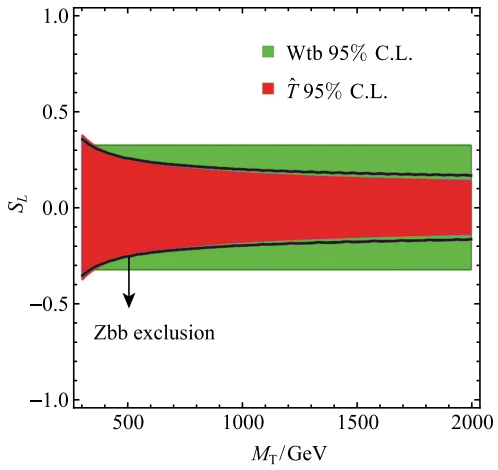

Fig. 14. (color online) Allowed parameter space at 95% C.L. of the Littlest Higgs with T parity model with $f=1$ TeV after including indirect and direct constraints. The convention is the same as in Fig. 9.

After considering the Wtb, Zbb and oblique $\hat{T}$ parameter experimental data, we plot in Fig. 14 the allowed parameter space of LHT model at 95% C.L. with $f = 1$ TeV in the $(s_L, M_{\rm T})$ plane.

We separate the constraints into different categories: the Wtb coupling constraint at 95% C.L. (green region), $\hat{T}$-parameter constraint at 95% C.L. (red region) and Zbb coupling constraint (black line).

From Fig. 14, we note that the bounds from $\hat{T}$ parameter and Zbb coupling are almost identical and are tighter than the bound from the Wtb coupling. None of the constraints are sensitive to the heavy T quark mass.

5 Discussion and conclusions

We have studied the top quark effective couplings using a set of higher dimensional operators made out of the SM fields. The leading contributions from NP can be captured by the dimension-six operators that are related to the top quark anomalous couplings $f_{1,2}^{L,R}$. Using the recent data of t-channel single top production σ_t, tW associated production $\sigma_{\rm tW}$, s-channel single top production σ_s and W-helicity fractions F_0, F_L and F_R collected at the 7 TeV, 8 TeV and 13 TeV LHC as well as at the Tevatron, we performed a global fit to impose constraints on the anomalous couplings $f_{1,2}^{L,R}$. The current data is sensitive to the top quark effective couplings and yields strong correlations among the top quark anomalous couplings.

We introduced x_0, x_p, x_m and x_5 (see Eq. (8)) to study the correlations among the top quark effective couplings. The variables x_i's are sensitive to the correlations among the top quark anomalous couplings; for example, x_m probes the correlation between f_1^L and f_2^R, x_p tests the correlation between f_1^R and f_2^L, x_5 is sensitive to the relation between f_2^L and f_2^R, and x_0 knows about all the four anomalous couplings. Precisely measuring the x_i's can probe the correlations among the top anomalous couplings, which may shed light on new physics models. We note that

(i) Improving the measurements of σ_t and $\sigma_{\rm tW}$ is important for constraining x_0, which can be translated into the correlation of (f_1^R, f_2^R) and (f_2^L, f_2^R); see Fig. 2(e) and Fig. 2(f).

(ii) x_m is sensitive to all the four experiments. As f_1^L and f_2^R are anti-correlated in x_m, reducing the uncertainty of x_m would tighten the correlation between f_1^L and f_2^R; see Fig. 2(c).

(iii) x_p is directly linked to the right-handed W-helicity fraction F_R, which is inferred from F_L and F_0 measurements. The strong anti-correlation between f_1^R and f_2^L is sensitive to the F_0 and F_L measurements; see Fig. 2(d).

(iv) x_5 is sensitive to the precision of σ_t, $\sigma_{\rm tW}$ and F_0 measurements.

At the 13 or 14 TeV LHC, the single top production cross sections increase and further affect the dependence of x_i's on the single top production and W-helicity fraction measurements. For example, the coefficients of σ_t and $\sigma_{\rm tW}$ decrease when the collider energy increases from 8 TeV to 13 or 14 TeV. The W-helicity fractions are measured in the top quark decay process, however, so the coefficients of F_0 and F_L remain almost the same as those at the 8 TeV LHC. Therefore, at the 13 or 14 TeV machine, the W-helicity fraction measurements play a more important role in determining x_i's. The x_i's can be better measured at the 13 or 14 TeV machine. More specifically, the F_0 measurement is important for the precision of the x_i's.

After exploring the allowed parameter space of those top quark effective couplings, we discussed their impact on the following three new physics models: the $G(221) = SU(2)_1 \otimes SU(2)_2 \otimes U(1)_X$, vector-like quark models and Littlest Higgs models with and without T-parity. These NP models modify the W-t-b coupling through gauge boson mixing or quark mixing if such a mixing is not forbidden by symmetry. For example, the W$'$ in the so-called $G(221)$ model can mix with the SM W-boson to affect the Wtb coupling; in the vector quark models new heavy quarks mix with the SM top quark or bottom quark to shift the Wtb coupling; in the Littlest Higgs model both gauge boson mixing and quark mixing are present. We translated our model-independent constraints of the top quark effective couplings into the parameter space of each new physics model.

Of the $G(221)$ models, we considered three typical models: the left-right model, the un-unified model and the top-flavor model. The structure of the Wtb coupling highly depends on the quantum number of top and bottom quarks under the $G(221)$ group and the symmetry breaking of $G(221) \to SU(2)_L \otimes U(1)_Y$. We showed that the Wtb coupling is sensitive to $\sin\phi$, which describes the ratio of gauge couplings in all $G(221)$ models except the top-flavour model when $M_{\rm W'}$ is less than several hundred GeV. In the left-right model we define $\tan\beta$ as the ratio of two vacuum expectation values. We note that the Wtb coupling is not sensitive to $\sin\beta$. The current experimental limits can be evaded if $M_{\rm W'}$ is larger than 2 TeV.

We considered seven kinds of vector quarks in this work: (i) weak singlet model: (T) quark and (B) quark; (ii) weak doublet model: (X,T), (T,B) and (B,Y); (iii) weak triplet models: (X,T,B) and (T,B,Y) model. The structure of the Wtb coupling depends strongly on the weak quantum number of vector quarks. We showed that the Wtb coupling is sensitive to the mixing angle s_L^t or s_L^b

in all the vector quark models except the (T,B) doublet model. To fully constrain the allowed parameter space of vector quark models, we included the constraints of oblique $\hat{T}$ parameter and Zbb couplings. We note that the $\hat{T}$ parameter and Zbb couplings impose much tighter constraints on the mixing angles than the effective Wtb couplings obtained from $\sigma_{s/t/tW}$ and $F_{0/L/R}$.

The Wtb coupling in the Littlest Higgs model is modified by both quark and gauge boson mixing. The Littlest Higgs model is severely constrained by W-W$'$ mixing at tree-level. We then considered the Littlest Higgs model with T-parity, which forbids the tree-level mixing of W and W$'$ bosons. The Wtb coupling is modified by the mixing of the top quark and top quark partner, which gives rise to constraints similar to the vector-like quark models.

The forthcoming LHC Run-II will collect more top quark pairs and single top quark events, which will improve the measurements of single top production and the W-helicity fraction. We expect tighter limits will be made on the effective top quark couplings and the dimension-six operators when new data is available. That will help us to probe new physics beyond the standard model.

References

1 G. Aad et al (ATLAS Collaboration), Phys. Lett., B, **716**: 1 (2012)
2 S. Chatrchyan et al (CMS Collaboration), Phys. Lett. B, **716**: 30 (2012)
3 F. Abe et al (CDF Collaboration), Phys.Rev. Lett., **74**: 2626 (1995)
4 S. Abachi et al (D0 Collaboration), Phys. Rev. Lett., **74**: 2632 (1995)
5 K. Hsieh, K. Schmitz, J.-H. Yu, and C.-P. Yuan, Phys. Rev. D, **82**: 035011 (2010)
6 Q.-H. Cao, Z. Li, J.-H. Yu, and C. Yuan, Phys. Rev. D, **86**: 095010 (2012)
7 F. del Aguila, M. Perez-Victoria, and J. Santiago, JHEP, **09**: 011 (2000)
8 J. A. Aguilar-Saavedra, JHEP, **11**: 030 (2009)
9 G. Cacciapaglia, A. Deandrea, D. Harada, and Y. Okada, JHEP, **1011**: 159 (2010)
10 J. Aguilar-Saavedra, R. Benbrik, S. Heinemeyer, and M. Victoria, Phys.Rev. D, **88**: 094010 (2013)
11 A. Belyaev, C.-R. Chen, K. Tobe, and C.-P. Yuan, Phys. Rev. D, **74**: 115020 (2006)
12 T. Han, H. E. Logan, B. McElrath, and L.-T. Wang, Phys. Rev. D, **67**: 095004 (2003)
13 F. Penunuri and F. Larios, Phys.Rev. D, **79**: 015013 (2009)
14 R. Contino, T. Kramer, M. Son, and R. Sundrum, JHEP, **0705**: 074 (2007)
15 A. Dabelstein, W. Hollik, C. Junger, R. A. Jimenez, and J. Sola, Nucl. Phys. B, **454**: 75 (1995)
16 J.-j. Cao, R. J. Oakes, F. Wang, and J. M. Yang, Phys. Rev. D, **68**: 054019 (2003)
17 B. Grzadkowski and W. Hollik, Nucl. Phys. B, **384**: 101 (1992)
18 A. Czarnecki, J. G. Korner, and J. H. Piclum, Phys. Rev. D, **81**: 111503 (2010)
19 CMS Collaboration (2013), CMS-PAS-TOP-13-008
20 ATLAS Collaboration (2013), ATLAS-CONF-2013-033, ATLAS-COM-CONF-2013-004
21 N. Kidonakis, Phys. Rev. D, **83**: 091503 (2011)
22 N. Kidonakis, Arxiv: 1205.3453
23 N. Kidonakis, Phys. Rev. D, **82**: 054018 (2010)
24 N. Kidonakis, Phys. Rev. D, **81**: 054028 (2010)
25 N. Kidonakis, URL https://inspirehep.net/record/1487920/files/arXiv:1609.07404.pdf
26 G. L. Kane, G. Ladinsky, and C. Yuan, Phys. Rev. D, **45**: 124 (1992)
27 E. Malkawi and C. Yuan, Phys. Rev. D, **50**: 4462 (1994)
28 D. O. Carlson, E. Malkawi, and C. Yuan, Phys. Lett. B, **337**: 145 (1994)
29 K. Whisnant, J.-M. Yang, B.-L. Young, and X. Zhang, Phys. Rev. D, **56**: 467 (1997)
30 J. M. Yang and B.-L. Young, Phys.Rev. D, **56**: 5907 (1997)
31 J.-J. Cao, J.-X. Wang, J. M. Yang, B.-L. Young, and X.-m. Zhang, Phys. Rev. D, **58**: 094004 (1998)
32 K.-i. Hikasa, K. Whisnant, J. M. Yang, and B.-L. Young, Phys. Rev. D, **58**: 114003 (1998)
33 F. Larios, M. Perez, and C. Yuan, Phys. Lett. B, **457**: 334 (1999)
34 Z. Lin, T. Han, T. Huang, J. Wang, and X. Zhang, Phys. Rev. D, **65**: 014008 (2002)
35 D. Espriu and J. Manzano, Phys. Rev. D, **65**: 073005 (2002)
36 C.-R. Chen, F. Larios, and C.-P. Yuan, Phys. Lett. B, **631**: 126 (2005)
37 P. Batra and T. M. Tait, Phys.Rev. D, **74**: 054021 (2006)
38 Q.-H. Cao, J. Wudka, and C.-P. Yuan, Phys. Lett. B, **658**: 50 (2007)
39 J. A. Aguilar-Saavedra, Nucl. Phys. B, **804**: 160 (2008)
40 E. L. Berger, Q.-H. Cao, and I. Low, Phys. Rev. D, **80**: 074020 (2009)
41 C. Zhang and S. Willenbrock, Phys. Rev. D, **83**: 034006 (2011)
42 J. A. Aguilar-Saavedra and J. Bernabeu, Nucl. Phys. B, **840**: 349 (2010)
43 S. D. Rindani and P. Sharma, JHEP, **1111**: 082 (2011)
44 S. D. Rindani and P. Sharma, Phys. Lett. B, **712**: 413 (2012)
45 F. Bach and T. Ohl, Phys. Rev. D, **86**: 114026 (2012)
46 M. Fabbrichesi, M. Pinamonti, and A. Tonero (2014), Arxiv: 1406.5393.
47 C. Bernardo, N. Castro, M. C. N. Fiolhais, H. Gonalves, A. G. C. Guerra et al, Arxiv: 1408.7063
48 I. Sarmiento-Alvarado, A. O. Bouzas, and F. Larios, Arxiv: 1412.6679
49 F. Bach and T. Ohl, Phys. Rev. D, **90**: 074022 (2014)
50 W. Buchmuller and D. Wyler, Nucl. Phys. B, **268**: 621 (1986)
51 R. Peccei and X. Zhang, Nucl.Phys. B, **337**: 269 (1990)
52 H. Georgi, Ann. Rev. Nucl. Part. Sci., **43**: 209 (1993)
53 F. Larios and C. Yuan, Phys. Rev. D, **55**: 7218 (1997)
54 T. M. Tait and C.-P. Yuan, Phys. Rev. D, **63**: 014018 (2000)
55 J. Aguilar-Saavedra, Nucl. Phys. B, **812**: 181 (2009)
56 J. Drobnak, S. Fajfer, and J. F. Kamenik, Phys. Rev. D, **82**: 114008 (2010)
57 C. Degrande, F. Maltoni, J. Wang, and C. Zhang, Phys. Rev. D, **91**: 034024 (2015)
58 C. Arzt, M. Einhorn, and J. Wudka, Nucl. Phys. B, **433**: 41 (1995)
59 C.-S. Li, J.-M. Yang, and B.-Q. Hu, Phys. Rev. D, **48**: 5425 (1993)
60 C. Arzt, Phys. Lett. B, **342**: 189 (1995)
61 The ATLAS collaboration (2013), ATLAS-CONF-2013-032
62 J. Pumplin, D. Stump, J. Huston, H. Lai, P. M. Nadolsky, et al, JHEP, **0207**; 012 (2002)
63 T. Stelzer, Z. Sullivan, and S. Willenbrock, Phys. Rev. D, **56**:

5919 (1997)
64 S. Zhu, Phys. Lett. B, **524**: 283 (2002)
65 B. Harris, E. Laenen, L. Phaf, Z. Sullivan, and S. Weinzierl, Phys. Rev. D, **66**: 054024 (2002)
66 J. M. Campbell, R. K. Ellis, and F. Tramontano, Phys. Rev. D, **70**: 094012 (2004)
67 Q.-H. Cao and C.-P. Yuan, Phys.Rev. D, **71**: 054022 (2005)
68 Q.-H. Cao, R. Schwienhorst, and C.-P. Yuan, Phys.Rev. D, **71**: 054023 (2005)
69 Q.-H. Cao, R. Schwienhorst, J. A. Benitez, R. Brock, and C.-P. Yuan, Phys. Rev. D, **72**: 094027 (2005)
70 J. M. Campbell, R. Frederix, F. Maltoni, and F. Tramontano, Phys. Rev. Lett., **102**: 182003 (2009)
71 S. Heim, Q.-H. Cao, R. Schwienhorst, and C.-P. Yuan, Phys. Rev. D, **81**: 034005 (2010)
72 R. Schwienhorst, C.-P. Yuan, C. Mueller, and Q.-H. Cao, Phys.Rev. D, **83**: 034019 (2011)
73 J. Wang, C. S. Li, and H. X. Zhu, Phys. Rev. D, **87**: 034030 (2013)
74 N. Kidonakis, Phys. Part. Nucl., **45**: 714 (2014)
75 T. A. Aaltonen et al (CDF Collaboration, D0 Collaboration), Phys. Rev. Lett., **112**: 231803 (2014)
76 T. A. collaboration (2015), ATLAS-CONF-2015-047
77 V. Khachatryan et al (CMS Collaboration), JHEP, **1406**: 090 (2014)
78 ATLAS collaboration (2014), ATLAS-CONF-2014-007, ATLAS-COM-CONF-2014-008
79 C. Collaboration (CMS) (2016), CMS-PAS-TOP-16-003
80 M. Aaboud et al (ATLAS) (2016), 1609.03920
81 CMS Collaboration (2014), CMS-PAS-TOP-14-009
82 T. A. collaboration (ATLAS) (2016)
83 F. James and M. Roos, Comput. Phys. Commun., **10**: 343 (1975)
84 B. Grzadkowski and M. Misiak, Phys. Rev. D, **78**: 077501 (2008)
85 W. Bernreuther, P. Gonzalez, and M. Wiebusch, Eur. Phys. J. C, **60**: 197 (2009)
86 K. Olive et al (Particle Data Group), Chin. Phys. C, **38**: 090001 (2014)
87 K. G. Chetyrkin, M. Misiak, and M. Munz, Phys. Lett. B, **400**: 206 (1997)
88 G. Burdman, M. Gonzalez-Garcia, and S. Novaes, Phys. Rev. D, **61**: 114016 (2000)
89 J. Drobnak, S. Fajfer, and J. F. Kamenik, Nucl. Phys. B, **855**: 82 (2012)
90 J. Drobnak, S. Fajfer, and J. F. Kamenik, Phys. Lett. B, **701**: 234 (2011)
91 R. Mohapatra and J. C. Pati, Phys. Rev. D, **11**: 2558 (1975)
92 R. N. Mohapatra and J. C. Pati, Phys. Rev. D, **11**: 566 (1975)
93 R. N. Mohapatra and G. Senjanovic, Phys. Rev. D, **23**: 165 (1981)
94 H. Georgi, E. E. Jenkins, and E. H. Simmons, Phys. Rev. Lett., **62**: 2789 (1989)
95 H. Georgi, E. E. Jenkins, and E. H. Simmons, Nucl. Phys. B, **331**: 541 (1990)
96 X. Li and E. Ma, Phys. Rev. Lett., **47**: 1788 (1981)
97 E. Malkawi, T. M. Tait, and C. Yuan, Phys. Lett. B, **385**: 304 (1996)
98 H.-J. He, T. M. Tait, and C. Yuan, Phys. Rev. D, **62**: 011702 (2000)
99 R. S. Chivukula, H.-J. He, J. Howard, and E. H. Simmons, Phys. Rev. D, **69**: 015009 (2004)
100 C. Du, H.-J. He, Y.-P. Kuang, B. Zhang, N. D. Christensen et al, Phys. Rev. D, **86**: 095011 (2012)
101 T. Abe, N. Chen, and H.-J. He, JHEP, **1301**: 082 (2013)
102 X.-F. Wang, C. Du, and H.-J. He, Phys. Lett. B, **723**: 314 (2013)
103 E. L. Berger, Q.-H. Cao, J.-H. Yu, and C.-P. Yuan, Phys. Rev. D, **84**: 095026 (2011)
104 J. Abdallah et al (DELPHI Collaboration), Eur. Phys. J. C, **60**: 1 (2009)
105 K. Agashe, R. Contino, L. Da Rold, and A. Pomarol, Phys. Lett. B, **641**: 62 (2006)
106 M. E. Peskin and T. Takeuchi, Phys. Rev. D, **46**: 381 (1992)
107 L. Lavoura and J. P. Silva, Phys. Rev. D, **47**: 2046 (1993)
108 C. Anastasiou, E. Furlan, and J. Santiago, Phys. Rev. D, **79**: 075003 (2009)
109 H. Cai, JHEP, **1302**: 104 (2013)
110 M. Baak et al (Gfitter Group), Eur. Phys. J. C, **74**: 3046 (2014)
111 V. Khachatryan et al (CMS), Arxiv: 1503.01952.
112 The ATLAS collaboration (2015), ATLAS-CONF-2015-012, ATLAS-COM-CONF-2015-012
113 M.-L. Xiao and J.-H. Yu, Phys. Rev. D, **90**: 014007 (2014)
114 N. Arkani-Hamed, A. Cohen, E. Katz, and A. Nelson, JHEP, **0207**: 034 (2002)
115 J. Reuter, M. Tonini, and M. de Vries, Arxiv: 1307.5010.
116 H.-C. Cheng and I. Low, JHEP, **0309**: 051 (2003)
117 H.-C. Cheng and I. Low, JHEP, **0408**: 061 (2004)
118 I. Low, JHEP, **0410**: 067 (2004)
119 J. Reuter, M. Tonini, and M. de Vries, JHEP, **1402**: 053 (2014)
120 J. Hubisz, P. Meade, A. Noble, and M. Perelstein, JHEP, **0601**: 135 (2006)